Die approbierte Originalversion dieser Diplom-/Masterarbeit ist in der Hauptbibliothek der Technischen Universität Wien aufgestellt und zugänglich.
http://www.ub.tuwien.ac.at

TU UB WIEN Universitätsbibliothek

The approved original version of this diploma or master thesis is available at the main library of the Vienna University of Technology.
http://www.ub.tuwien.ac.at/eng

TECHNISCHE
UNIVERSITÄT
WIEN
Vienna University of Technology

DIPLOMARBEIT

MODE BASIS APPROACH TO QUANTUM TRANSPORT CALCULATIONS

Ausgeführt am Institut für Theoretische Physik
der Technischen Universität Wien
unter der Anleitung von

O.UNIV.PROF. DIPL.-PHYS. DR.RER.NAT.
JOACHIM BURGDÖRFER
und
ASSISTANT PROF. DIPL.-ING. DR.TECHN.
FLORIAN LIBISCH

durch
THOMAS FABIAN, BSC.
Baumeistergasse 93/5, 1160 Wien

Wien, 15.05.2017

> IL SEMBLE QUE LA PERFECTION SOIT ATTEINTE
> NON QUAND IL N'Y A PLUS RIEN À AJOUTER,
> MAIS QUAND IL N'Y A PLUS RIEN À RETRANCHER
>
> ANTOINE DE SAINT EXUPÉRY[1]

THOMAS FABIAN

MODE BASIS APPROACH TO QUANTUM TRANSPORT CALCULATIONS

May 17, 2017

This thesis is typeset in LaTeX which was developed by Leslie Lamport [16] and is based on TeX by Donald Knuth [15]. The Memoir class by Peter Wilson [30] is used. Kp-fonts-light by Christophe Caignaert [4] based on Palatino by Hermann Zapf are chosen to achieve an elegant yet fragile look. Figures are drawn with the tikz[26] and the pgfplots[8] packages. The page layout is inspired by the works of Edward Tufte , e.g. *Beautiful Evidence*[27]. The small textblock width ensures good readability and the ample margins allow for additional comments. Chapter headings are similar to those found in Robert Bringhurst 's *Elements of Typographic Style*[3].

Contents

Contents V

Acknowledgements IX

Deutsche Kurzfassung XI

Abstract XIII

1 *Introduction* 1

1.1 *Mode basis in the literature* 2

2 *Background* 3

2.1 LANDAUER-BÜTTIKER *formalism* 3

2.2 BEUTLER-FANO *resonances* 4

2.3 *Graphene* 5

2.4 *Tight Binding for Graphene* 6

2.5 GREEN *'s functions* 9

3 *Mode basis* 13

3.1 *Transverse modes* 13

3.2 *Eigenfunctions of an infinite lead* 14

3.3 *Definition of the mode basis* 16

3.4 *Recursive* GREEN *'s function method* 18

4 *Computations in the Mode basis* 25

4.1 *Timing* 25

4.2 *Building Blocks* 26

4.3 *Resonances* 30

4.4 Magnetic Field 32

5 Phonons 35

5.1 Electron - Phonon interaction 35

5.2 Mode Opening 37

5.3 Random Walk model 39

5.4 Building Blocks 41

5.5 Towards a more realistic phonon model 47

6 Conclusion & Outlook 51

A Things that do not work 53

A.1 Expansion in Phonon Coupling 53

A.2 Alternative: Phonon Coupling over H_I 53

References 55

⁂

Acknowledgements

It is impossible to write a thesis without the encouragement and support of many people. I'm especially grateful to my supervisor Florian Libisch, not only for always being open for questions and ready to help, but also for being such a dedicated researcher and therefore an important role model. I would like to thank Joachim Burgdörfer for valuable suggestions and discussions. Furthermore I would like to thank my colleagues, Lukas Linhart, Tobias Jawecki, Isabella Floss, Christoph Schattauer, Valerie Smejkal, Schlomo Bambusek, David Erkinger, Tobias Reisch ..., for interesting discussions, support and friendship. I am very happy to be part of the research group of Joachim Burgdörfer, where such a friendly and supportive atmosphere prevails. I would like to thank my parents Irmgard & Wolfgang Fabian for their support and for proof-reading.

I would like to cordially invite all of you to the tea room for a Sacher torte according to a family recipe.

Sachertorte

200 g butter
200 g sugar
200 g chocolate
200 g flour
6 eggs
*2 strawberries**
Apricot Glaze
Chocolate Glaze

Melt the chocolate in a bain-marie. Beat the butter until smooth, then slowly beat in the sugar, the chocolate, and egg yolks. Beat the egg whites. Add a tablespoon of sugar and mix. Add the egg whites to the chocolate mixture, sift the flour over it, then carefully fold it into the mixture.
Bake until a toothpick inserted in the center comes out clean, about 45 minutes. Cool completely. Cut the cake into two layers, and brush each layer with apricot glaze. Assemble and let the glaze set. Finally, pour the warm chocolate glaze on top of the cake and smooth.

**Add the secret ingredient at a plausible step.*

Deutsche Kurzfassung

Diese Arbeit stellt eine approximative, höchst effiziente Methode zur Berechnung von Quantentransport-Simulationen vor. Dabei wird das Streuproblem auf die flusstragenden und ausgewählte geschlossene Moden, den Eigenfunktionen eines Wellenleiters, projiziert. Dadurch reduziert sich die Systemgröße beachtlich, und Berechnungen können sehr effizient ausgeführt werden. Der vorgestellte und implementierte Algorithmus eignet sich im Besonderen für nicht-separable Hamilton -operatoren, was eine Neuerung darstellt.

Wir testen unseren Algorithmus an Graphenstrukturen. Einfache Geometrien und schwache Magnetfelder können in sehr guter Übereinstimmung mit exakten Rechnungen beschrieben werden. Wenn jedoch die zugrundeliegende Annahme von Fluss in eine Richtung und Quantisierung in die anderen Richtungen verletzt ist, lässt sich die Näherung nicht mehr anwenden.

Die Effizienz der Methode erlaubt nun die Gleichungen für einen diskreten Satz von Energien zu koppeln. Damit kann inelastische Elektron-Phonon Streuung an optischen Phononen modelliert werden. In den resultierenden Transmissionskurven werden weiche Maxima generell weiter verbreitert. Scharfe Spitzen erscheinen mehrmals, jeweils korrespondierend zu einer Phononenkonfiguration. Minima in der Transmission bleiben unbeeinflusst.

Diese Arbeit ist ein Schritt zum Verständnis realistischer Bedingungen in Experimenten an vollständig kohärenten quantenmechanischen Systemen.

Abstract

In this thesis we present an approximate but highly efficient method for quantum transport calculations. Our approach is based on the eigenstates of the infinite waveguide, the so-called modes. By projecting the scattering problem onto the propagating and selected evanescent modes, we reduce the system size and improve the speed drastically. We find and implement a numerically stable procedure even for non-separable HAMILTONIANS , which has not been done before.

We test our algorithm on graphene scattering structures. For simple geometries and weak magnetic fields, the approximation is in very good agreement with the exact calculations. The mode-basis approach is not valid whenever the assumption of propagation in one direction and quantized modes in the other direction fails.

We exploit the speed of the mode basis to couple the equations for a discrete set of energies spaced $E = \hbar\omega$ apart. This serves as a model for inelastic electron-phonon scattering on optical phonons with frequency ω. We find that resulting transmission curves typically get smeared out, as peaks in the transmission curve now appear multiple times. Conversely, dips in the transmission remain unaffected.

This work is a step towards understanding the effects of realistic experimental conditions on ideally fully coherent quantum mechanical systems.

⁂

Introduction

1

Consider an idealized Coulomb Blockade measurement, as sketched in Fig. 1.1. We contact a quantum dot with source at potential V_1 and drain at potential V_2. Whenever there is an unoccupied energy level in the bias voltage window $V_1 > E > V_2$, an electron can traverse the quantum dot and current is measured. The energy levels in the dot can be shifted by changing the gate voltage V_g.

In a standard numerical simulation, the scattering matrix of a system with Hamiltonian $\mathcal{H}$ is calculated via the Green's function $\mathcal{G} = 1/(E - \mathcal{H})$ at fixed energy E.

In any real experiment however, we have to deal with finite temperatures. A Fermi distribution then describes the occupation in the source and drain. Further, an electron may undergo inelastic scattering. One might, in a more realistic model, want to let the electron scatter into i possible energies $E' \neq E$, as sketched in Fig. 1.2. This requires solving the coupled equations for multiple energies. Instead of a system consisting of N atomic orbitals, the system is now of size $i \cdot N$. Is this numerically feasible? It turns out not since the computational time for the problem goes with $\mathcal{O}\left(n^{3.8}\right)$, see Section 4.1. Even a moderately small system becomes unfeasible when coupling more than $i \gtrsim 4$ energies.

We thus have to search for a suitable approximation. The first idea which usually comes to mind is a Taylor expansion. The presumably small coupling between the different energies seems like an ideal expansion parameter. The equations decouple when restricted to first order, as shown in Appendix A. This approach however turns out to be numerically unstable.

A projection on the flux-carrying modes reduces the system size drastically. A few coupled equations are then not a problem any longer. In this thesis we propose to use the mode basis approach for approximate, but efficient, quantum transport calculations. The mode basis is already used in a few quantum simulation codes, see Section 1.1, but has (to our knowledge) not been applied to non-separable Hamiltonians (see Section 3.3).

Outline This thesis is organized as follows. We use the preparatory Chapter 2 to introduce the Landauer-Büttiker formalism, Green's functions and graphene. The mode basis is defined in Chapter 3, where we also give the equations to obtain reflection and transmission coefficients. The questions "How fast is this approximation?" and "How much of an approximation is it?" are answered in Chapter 4. We exploit the potential of the mode basis in Chapter 5. We model inelastic scattering at optical phonons with energy $\hbar\omega$, and couple multiple energies spaced $\hbar\omega$ apart.

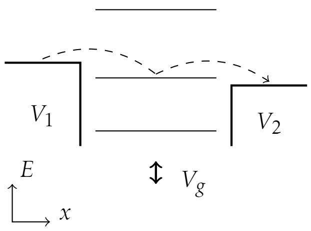

Figure 1.1: Idealized Coulomb blockade measurement. Source and drain are at potential V_1 and V_2, and the energy levels of the quantum dot can be tuned with V_g.

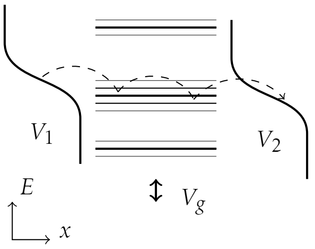

Figure 1.2: In a more realistic scenario, an electron may undergo inelastic scattering inside the quantum dot. At finite temperature, the occupation of source and drain are described by the Fermi distribution.

1.1 *Overview of mode basis approach in the literature*

It is well known that quantities related to (semi-) infinite leads can often be analytically written down in the mode basis. Usually, one immediately transforms these quantities into the position basis. We want to give a partial overview of few works which use the mode basis explicitly.

In 2003 in the paper *"Towards Multi-Scale Modeling of Carbon Nanotube Transistors"* GUO et al.[13] use the M circumferential modes contributing to transport in carbon nanotubes as their basis. This decouples the nearest neighbour tight binding HAMILTONIAN into M one-dimensional problems. The mode space approach for carbon nanotubes has since been used multiple times.

For the continuum limit/effective mass HAMILTONIAN , which can, for example be used to describe silicon nanowire transistors, the mode basis approach is well established, see *"A Three-Dimensional Quantum Simulation of Silicon Nanowire Transistors with the Effective-Mass Approximation"* by WANG et al.[28] or *"Quantum transport in two- and three-dimensional nanoscale transistors: Coupled mode effects in the nonequilibrium Green's function formalism"* by LUISIER et al.[20]

In a series of articles GRASSI et al. [10, 11] apply the mode space approach to graphene nanoribbons. They show that the (full) mode basis decouples, under certain circumstances, into different groups. The modes are defined as the eigenfunctions at $k = 0$ of a slab (or the periodic repetition of it) in the nearest neighbour approximation.

In contrast to the above approach we use the more accurate third-nearest neighbour HAMILTONIAN as starting point, and we do not solve for all modes. A (truncated) mode basis calculation of a non-separable tight binding HAMILTONIAN is (to our knowledge) presented for the first time.

The decisive hint which finally stabilized the computation actually came from an experimental paper, *"Signatures of evanescent mode transport in graphene"* by WIENER et al.[29]. This article reveals the importance of evanescent modes in graphene. The numerical simulation requires the inclusion of multiple evanescent modes, in contrast to the continuum limit HAMILTONIAN .

As a side remark, even the exact calculation becomes unstable when one projects the GREEN *'s functions on the open modes at one point in the calculation.*

❖

Background

2

This chapter is intended as a bridge between basic quantum mechanics and the field of quantum transport. It contains mostly textbook knowledge, but is included for later reference and to establish naming conventions. We start with an overview of the LANDAUER-BÜTTIKER *formalism in Section 2.1. Transmission curves inevitably contain resonances, which we discuss in Section 2.2. In Section 2.3, we introduce graphene. We calculate the band structure of graphene in Section 2.4.* GREEN *'s function are introduced in Section 2.5, with special focus on their use in quantum transport calculations.*

2.1 LANDAUER-BÜTTIKER *formalism*

We calculate the current flowing trough a conductor. An electron gas with density n and velocity v carries a current $j = env$. The density per unit length of a single k state in a specific mode in a conductor of length L is $1/L$. Suppose this state is occupied according to a function $f^+(E)$. The current carried by this state is

$$I = \frac{e}{L} v f^+(E) \overset{\rightarrow}{=} \frac{e}{L}\frac{1}{\hbar}\frac{\partial E}{\partial k} f^+(E)$$

We recapitulate the LANDAUER-BÜTTIKER *formalism by following the beautiful exposition* "Electronic Transport in Mesoscopic Systems" *by* DATTA *[5]. Following up on that, we incorporate a transmission function which allows coupling between different energies. This becomes important in Chapter 5, where we describe inelastic scattering.*

Summing over all $+k$ states in the specific mode gives

$$I = \frac{2e}{h}\int_{\epsilon}^{\infty} f^+(E)\,\mathrm{d}E$$

As usual, we convert the sum over the $+k$ states into an integral

$$\sum_k = \frac{gL}{2\pi}\int \mathrm{d}k$$

We extend this result to a multi-mode waveguide by introducing the function $M(E) = \sum_n \Theta(E - \epsilon_n)$, which counts the number of open modes.

$$I = \frac{2e}{h}\int_{\epsilon}^{\infty} f^+(E) M(E)\,\mathrm{d}E$$

To continue, we assume the contacts to the right and left of the conductor are held at electrochemical potentials μ_1 and μ_2, respectively. Furthermore, we assume that electrons can enter the conductor reflectionless. Since all right-propagating modes come from the left contact, the right-propagating modes in the left lead have a potential of μ_1. Similarly, all left-propagating modes in the right lead have a potential of μ_2. In the limit of zero temperature we thus have an influx from the left lead given by

In order to support the assumption of reflectionless contacts imagine a waveguide which opens up into a much larger region, the conductor. Intuitively, all modes will be able to enter the wider region without significant backscattering. For a more throughout discussion, see [5].

$$I_1^+ = \frac{2e}{h} M(E)\,(\mu_1 - \mu_2).$$

For a device with transmission T, the outflux into lead 2 is then $I_2^+ = TI_1^+$, and the flux back into lead 1 is given by $I_1^- = (1-T)I_1^+$. The net current in the device is $I_1^+ - I_1^- \equiv I_2^+ = TI_1^+$. The conductance G is

$$G = \frac{I}{(\mu_1 - \mu_2)/|e|} \overset{\rightarrow}{=} \frac{2e^2}{h} MT \tag{2.1}$$

When we restore temperature effects and consider a mode-dependent transmission function $T_i(E)$, we have

$$I = \frac{2e}{h}\int_{-\infty}^{\infty}\sum_{i}^{M(E)}\left(f^{+}(E-\mu_L)-f^{+}(E-\mu_R)\right)T_i(E)\,\mathrm{d}E.$$

In this thesis, we also investigate the effect of inelastic scattering by the current carrying electrons. The transmission becomes a function of the ingoing energy E and the outgoing energy E', $T(E,E')$. We can now compare with experiments at finite temperature and inelastic scattering,

$$I = \frac{2e}{h}\iint_{-\infty}^{\infty}\mathrm{d}E\,\mathrm{d}E'\sum_{i}^{M(E)}\sum_{j}^{M(E')}\left(f^{+}(E-\mu_L)-f^{+}(E'-\mu_R)\right)T_{ij}(E,E')$$

The formula for $T_{ij}(E,E')$ is derived in Chapter 3.

2.2 Beutler-Fano *resonances*

In this section, we follow the review paper “Fano resonances in nanoscale structures”*[22] by* Miroshnichenko *et al.*

The transmission curve as a function of energy of a scattering structure is typically a complicated curve with various peaks and dips. They can be understood with a formula put forward by Fano [6]. Its main ingredient is the quantum interference between scattering within a continuum of states and resonant scattering with a discrete state.

Historically, Fano considered the absorption spectra of noble gases measured by Beutler. The direct ionization process of atoms A by photons of energy $E = h\nu$ is described by $h\nu + A \rightarrow A^{+} + e^{-}$. Emission via the Auger process is another possible process. In a first step, the atom is excited to an autoionizing state A^{*}, and released into the continuum in a second step, $h\nu + A \rightarrow A^{*} \rightarrow A^{+} + e^{-}$.

In quantum transport experiments, the infinite lead provides the continuum of states, while the scattering structure has a set of discrete eigenstates. To be more precise, the discrete energy levels of the scattering structure without leads get broadened by the coupling to the leads.

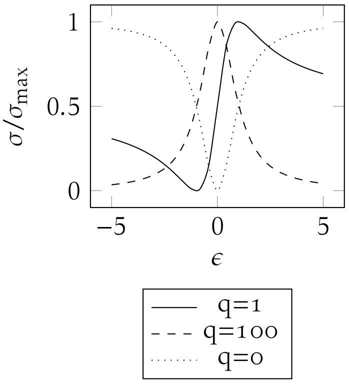

Figure 2.1: Normalized Fano *profiles for various values of the asymmetry parameter q.*

In both cases, amplitude and phase of the scattering into the continuum typically vary slowly, but they change quickly for the resonant process. This superposition leads to the asymmetric Fano line shape. As formula, Fano [6] introduced the scattering cross section

$$\sigma(\epsilon) = \frac{(\epsilon - q)^2}{\epsilon^2 + 1},$$

where ϵ is a reduced energy $\epsilon = 2(E - E_F)/\Gamma$, with energy E_F and width Γ of the discrete state, and q a phenomenological shape parameter.

Enlightening is the decomposition given in [22]

$$\underbrace{\frac{q^2-1}{\epsilon^2+1}}_{\text{discrete}} + \underbrace{\frac{2q\epsilon}{\epsilon^2+1}}_{\text{mixing}} + \underbrace{1}_{\text{continuum}} = \frac{(\epsilon-q)^2}{\epsilon^2+1}$$

of the Fano line shape into a Lorentzian line shape of the discrete state and the continuum.

For large q, we recover the line shape of the Breit-Wigner distribution. In this case, tunneling through the resonant state is the dominating process. When $q \approx 1$, the continuous and resonant process are of the same strength. The Fano profile is maximally asymmetric. For small q, the formula describes a symmetric dip, a so-called window resonance, see Fig. 2.1.

One can tune this parameter in an actual experiment, see for example *"Tunable Fano Resonances in Transport through Microwave Billiards"*[24] by Rotter et al.: In a microwave scattering device, the coupling of a cavity to the leads is controlled by two diaphragms. For fully open leads, window resonances can be observed and identified with eigenstates of the closed cavity. By closing the diaphragms, the transition of these resonances via a Fano profile towards sharp Lorentzian peaks which occur at eigenvalues of the close cavity can be observed.

Let us close this section with a neat toy model given by Joe et al in *"Classical analogy of Fano resonances"*[14]. Consider two coupled harmonic oscillators with frequencies ω_1, ω_2, damping γ_1 and γ_2 and coupling v_{12}. The first oscillator is driven. The equations of motion read

$$\begin{aligned} \ddot{x}_1 + \gamma_1 \dot{x}_1 + \omega_1^2 x_1 + v_{12} x_2 &= a_1 \mathrm{e}^{\mathrm{i}\omega t}, \\ \ddot{x}_2 + \gamma_2 \dot{x}_2 + \omega_2^2 x_2 + v_{12} x_1 &= 0. \end{aligned}$$

The stationary solution can be found with the ansatz

$$x_1 = c_1 \mathrm{e}^{\mathrm{i}\omega t}, \qquad x_2 = c_2 \mathrm{e}^{\mathrm{i}\omega t}.$$

The solutions for the amplitudes are

$$\begin{aligned} c_1 &= \frac{\omega_2^2 - \omega^2 + \mathrm{i}\gamma_2\omega}{\left(\omega_1^2 - \omega^2 + \mathrm{i}\gamma_1\omega\right)\left(\omega_2^2 - \omega^2 + \mathrm{i}\gamma_2\omega\right) - v_{12}^2} a_1, \\ c_2 &= -\frac{v_{12}}{\left(\omega_1^2 - \omega^2 + \mathrm{i}\gamma_1\omega\right)\left(\omega_2^2 - \omega^2 + \mathrm{i}\gamma_2\omega\right) - v_{12}^2} a_1. \end{aligned}$$

The peaks appear close – the coupling v_{12} induces a small shift – to the eigenfrequencies ω_1 and ω_2 . The width of the peaks is determined by the imaginary part of the eigenfrequencies. In absence of damping, $\gamma_2 = 0$, the amplitude c_1 is zero for $\omega = \omega_2$. This introduces the asymmetry in the peak near ω_2 in this model, see Fig. 2.2.

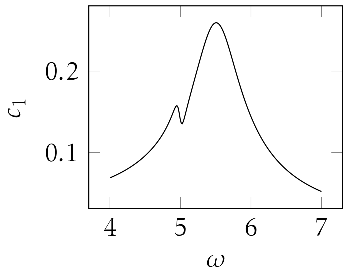

Figure 2.2: Amplitude c_1 of a driven harmonic oscillator with frequency $\omega_1 = 5.5 + 0.3\mathrm{i}$ with damping $\gamma_1 = 0.1$, coupled to a harmonic oscillator with frequency $\omega_2 = 5$ and damping $\gamma = 0.1$ with coupling strength $v_{12} = 1$.

2.3 Graphene

In this thesis we will describe electronic transport calculations with special focus on graphene nanostructures. The carbon atoms in graphene form a honeycomb lattice. The underlying Bravais lattice is a hexagonal lattice. The unit cell contains two atoms, labeled as "A" and "B". A carbon atom has 2 core electrons and 4 valence electrons

For more information, see Electronic properties of monolayer and bilayer graphene *by* McCann *[21].*

in the $2s$, $2p_x$, $2p_y$, and $2p_z$ orbitals. The former three hybridize and form sp^2 orbitals. Graphene takes its physical strength from the sigma bonds between adjacent carbon atoms. The electronic properties are determined by the remaining $2p_z$ orbitals, which lie perpendicular to the graphene plane.

2.4 Tight Binding for Graphene

The numerical calculations in this thesis are done in the tight binding approximation. A physical system is represented by a matrix, where the basis functions are the relevant atomic orbitals. Of interest is also the slightly unusual band structure of graphene. For a derivation of the tight binding approximation, see "Solid State Physics" *by* GROSSO *and* PARRAVICINI, *[12].*

Let us calculate the band structure of graphene. In the tight-binding model we calculate the electronic band structure of a solid using a set of wave-functions consisting of localized atomic orbitals. The idea one has in mind is that one describes tightly bound electrons with occasional hopping between different sites. We write our electron wave function $\Phi_i(\boldsymbol{r})$ at position $\boldsymbol{r}$ of orbital i as a linear combination of localized orbitals $\phi_i(\boldsymbol{r}-\boldsymbol{R})$ at various lattice points $\boldsymbol{R}$. BLOCH's theorem tells us that energy eigenstates of an electron in a solid can be written as $\Phi_{\boldsymbol{k},i}(\boldsymbol{r}-\boldsymbol{R}) = \exp(\mathrm{i}\boldsymbol{k}\boldsymbol{R})\Phi_{\boldsymbol{k},i}(\boldsymbol{r})$, where $\boldsymbol{k}$ takes on the N values in the first BRILLOUIN zone. This fixes the coefficients of the linear expansion to

$$\Phi_{\boldsymbol{k},i}(\boldsymbol{r}) = \frac{1}{\sqrt{N}}\sum_{\boldsymbol{R}} \mathrm{e}^{\mathrm{i}\boldsymbol{k}\boldsymbol{R}}\phi_i(\boldsymbol{r}-\boldsymbol{R}).$$

Since graphene has two atoms in the unit cell, each with one p_z shell which we want to include, the wavefunction is a linear combination of the two BLOCH sums corresponding to the A and B sublattices,

$$\psi(\boldsymbol{k},\boldsymbol{r}) = \alpha\Phi_A(\boldsymbol{k},\boldsymbol{r}) + \beta\Phi_B(\boldsymbol{k},\boldsymbol{r}).$$

We also expect two energy bands, $i = 1, 2$. Let us now calculate the relevant matrix elements. We will work in the nearest neighbour approximation. Let us normalize the states according to

$$\langle\phi_A(\boldsymbol{r}-\boldsymbol{R}_A)\big|\phi_A(\boldsymbol{r}-\boldsymbol{R}_A)\rangle = \langle\phi_B(\boldsymbol{r}-\boldsymbol{R}_B)\big|\phi_B(\boldsymbol{r}-\boldsymbol{R}_B)\rangle = 1.$$

The on-site energy is

$$\epsilon_{2p} := \langle\phi_A(\boldsymbol{r}-\boldsymbol{R}_A)\big|\mathcal{H}\big|\phi_A(\boldsymbol{r}-\boldsymbol{R}_A)\rangle = \langle\phi_B(\boldsymbol{r}-\boldsymbol{R}_B)\big|\mathcal{H}\big|\phi_B(\boldsymbol{r}-\boldsymbol{R}_B)\rangle,$$

which has the same value for each lattice site. The hopping element between $\boldsymbol{R}_A$ and neighbouring atoms $\boldsymbol{R}_B$ is

$$H_{AB} := \sum_{\boldsymbol{R}_B} \mathrm{e}^{\mathrm{i}\boldsymbol{k}(\boldsymbol{R}_B-\boldsymbol{R}_A)}\langle\Phi_A(\boldsymbol{r}-\boldsymbol{R}_A)|\mathcal{H}|\Phi_B(\boldsymbol{r}-\boldsymbol{R}_B)\rangle$$

We define $\gamma_0 := -\langle\Phi_A(\boldsymbol{r}-\boldsymbol{R}_A)|\mathcal{H}|\Phi_B(\boldsymbol{r}-\boldsymbol{R}_B)\rangle$. The relative position vector $\boldsymbol{\delta}_l = \boldsymbol{R}_{B,l} - \boldsymbol{R}_A$ between an A-atom and the $l = 1, 2, 3$ neighbouring B-atoms are

$$\boldsymbol{\delta}_1 = \begin{pmatrix} 0 \\ a/\sqrt{3} \end{pmatrix}, \qquad \boldsymbol{\delta}_2 = \begin{pmatrix} a/2 \\ -a/(2\sqrt{3}) \end{pmatrix}, \qquad \boldsymbol{\delta}_3 = \begin{pmatrix} -a/2 \\ -a/(2\sqrt{3}) \end{pmatrix}.$$

The sum over the exponential can readily be calculated:

$$\begin{aligned} f(\boldsymbol{k}) &:= \sum_{l=1}^{3} \mathrm{e}^{\mathrm{i}\boldsymbol{k}\boldsymbol{\delta}_l} \\ &= \mathrm{e}^{\mathrm{i}k_y a/\sqrt{3}} + \mathrm{e}^{\mathrm{i}k_x a/2}\mathrm{e}^{-\mathrm{i}k_y a/\sqrt{3}} + \mathrm{e}^{-\mathrm{i}k_x a/2}\mathrm{e}^{-\mathrm{i}k_y a/\sqrt{3}} \\ &= \mathrm{e}^{\mathrm{i}k_y a/\sqrt{3}} + 2\mathrm{e}^{-\mathrm{i}k_y a/\sqrt{3}}\cos(k_x a/2). \end{aligned}$$

Putting it all together, we arrive at (assuming time reversal symmetry and hence $\gamma_0 \in \mathfrak{Re}$)

$$H_{AB} = -\gamma_0 f(\boldsymbol{k}), \qquad H_{BA} = H_{AB}^* = -\gamma_0 f^*(\boldsymbol{k})$$

The calculation for the overlap matrix proceeds similarly

$$\begin{aligned} S_{AB} &:= \sum_{\boldsymbol{R}_B} \mathrm{e}^{\mathrm{i}\boldsymbol{k}(\boldsymbol{R}_B-\boldsymbol{R}_A)} \langle \Phi_A(\boldsymbol{r}-\boldsymbol{R}_A) | \Phi_B(\boldsymbol{r}-\boldsymbol{R}_B) \rangle \\ &=: s_0 f(\boldsymbol{k}) \\ S_{BA} &= s_0 f^*(\boldsymbol{k}), \end{aligned}$$

where we have defined $s_0 = \langle \Phi_A(\boldsymbol{r}-\boldsymbol{R}_A) | \Phi_B(\boldsymbol{r}-\boldsymbol{R}_B) \rangle$ in the second line.

Now we are ready to calculate the energy

$$E_{\boldsymbol{k}} = \frac{\langle \psi_{\boldsymbol{k}} | \mathcal{H} | \psi_{\boldsymbol{k}} \rangle}{\langle \psi_{\boldsymbol{k}} | \psi_{\boldsymbol{k}} \rangle}$$

by inserting $\psi(\boldsymbol{k}, r) = \alpha\Phi_A(\boldsymbol{k}, r) + \beta\Phi_B(\boldsymbol{k}, r)$ into the above equation,

$$E_{\boldsymbol{k}} = \frac{\left(\alpha^2+\beta^2\right)\epsilon_{2p} - \alpha^*\beta\gamma_0 f(\boldsymbol{k}) - \alpha\beta^*\gamma_0 f^*(\boldsymbol{k})}{(\alpha^2+\beta^2) + \alpha^*\beta s_0 f(\boldsymbol{k}) - \alpha\beta^* s_0 f^*(\boldsymbol{k})}.$$

In the following, we determine α and β by a variational principle.

α and β are not independent, as they determine the norm of the vector ψ. Out of the remaining free parameters, it is easiest to vary with respect to α^* and β^*.

$$\frac{\partial E_{\boldsymbol{k}}}{\partial \alpha^*} = \frac{\alpha\epsilon_{2p} - \beta\gamma_0 f(\boldsymbol{k})}{\langle \psi_{\boldsymbol{k}} | \psi_{\boldsymbol{k}} \rangle} + \frac{\langle \psi_{\boldsymbol{k}} | \mathcal{H} | \psi_{\boldsymbol{k}} \rangle}{\langle \psi_{\boldsymbol{k}} | \psi_{\boldsymbol{k}} \rangle} \frac{\alpha + \beta s_0 f(\boldsymbol{k})}{\langle \psi_{\boldsymbol{k}} | \psi_{\boldsymbol{k}} \rangle}$$

We now set $\partial E/\partial\alpha^* = 0$, cancel the common denominator and note that the second term contains the expression for the energy. This leads to

$$\alpha\epsilon_{2p} - \beta\gamma_0 f(\boldsymbol{k}) = E_{\boldsymbol{k}}(\alpha + \beta s_0 f(\boldsymbol{k})).$$

Varying with respect to β^* yields

$$\beta\epsilon_{2p} - \alpha\gamma_0 f^*(\boldsymbol{k}) = E_{\boldsymbol{k}}(\beta + \alpha s_0 f^*(\boldsymbol{k})).$$

Putting this into matrix form, we have

$$\begin{pmatrix} \epsilon_{2p} & -\gamma_0 f(\boldsymbol{k}) \\ -\gamma_0 f^*(\boldsymbol{k}) & \epsilon_{2p} \end{pmatrix} \begin{pmatrix} \alpha \\ \beta \end{pmatrix} = E_{\boldsymbol{k}} \begin{pmatrix} 1 & s_0 f(\boldsymbol{k}) \\ s_0 f^*(\boldsymbol{k}) & 1 \end{pmatrix} \begin{pmatrix} \alpha \\ \beta \end{pmatrix}.$$

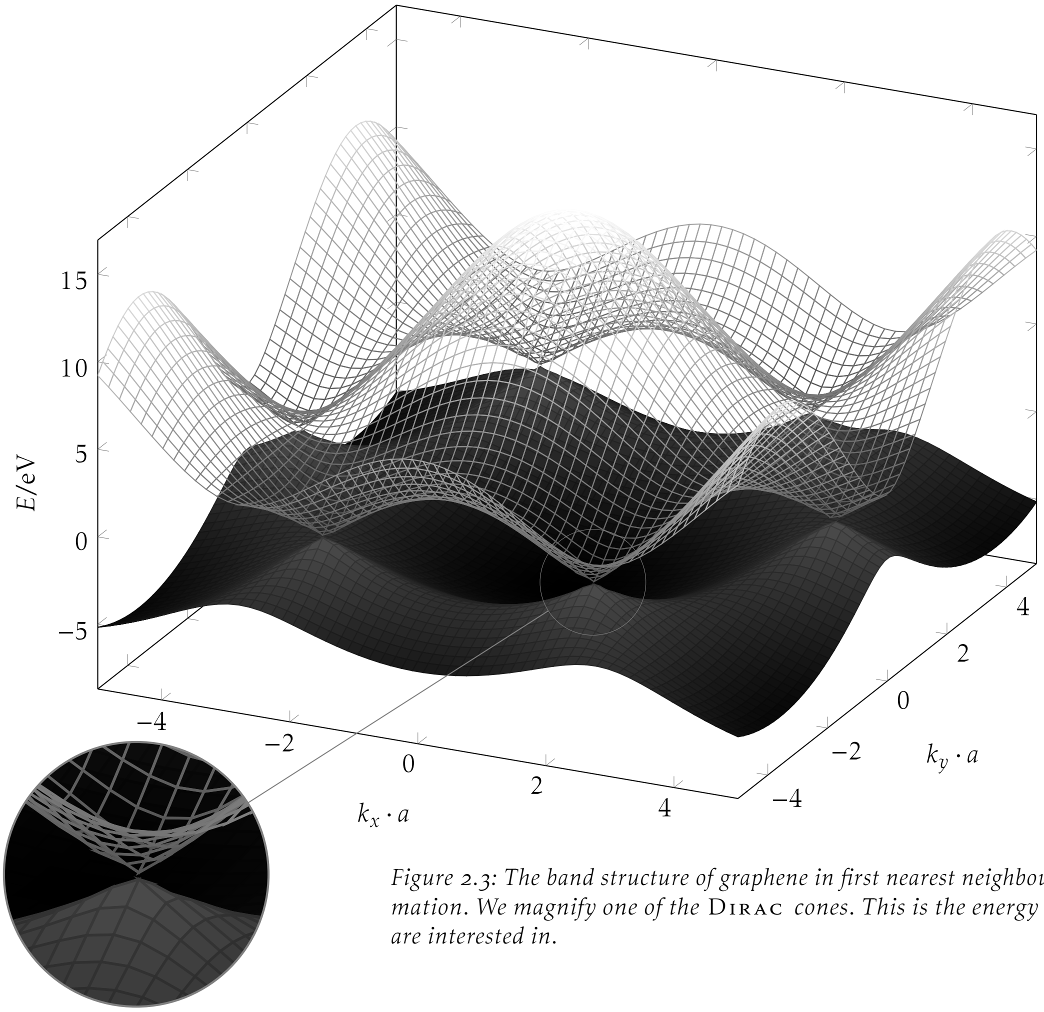

Figure 2.3: The band structure of graphene in first nearest neighbour approximation. We magnify one of the DIRAC *cones. This is the energy regime we are interested in.*

We continue to solve for the energy,

$$\det\begin{pmatrix} \epsilon_{2p} - E_{\boldsymbol{k}} & -(\gamma_0 + E_{\boldsymbol{k}} s_0) f(\boldsymbol{k}) \\ -(\gamma_0 + E_{\boldsymbol{k}} s_0) f^*(\boldsymbol{k}) & \epsilon_{2p} - E_{\boldsymbol{k}} \end{pmatrix} = 0$$

$$\left(E_{\boldsymbol{k}} - \epsilon_{2p}\right)^2 - (\gamma_0 + E_{\boldsymbol{k}} s_0)^2 \left|f(\boldsymbol{k})\right| = 0.$$

The two solutions to this equation are

$$E_{\boldsymbol{k},\pm} = \frac{\epsilon_{2p} \pm \gamma_0 \left|f(\boldsymbol{k})\right|}{1 \mp s_0 \left|f(\boldsymbol{k})\right|}.$$

We plot the resulting band structure in Fig. 2.3.

2.5 GREEN *'s functions*

By the superposition principle we know that a wavefunction $\psi(x')$ at $x' = (\boldsymbol{x}', t')$, with position $\boldsymbol{x}'$ and time t', can be written as the sum of spherical outward traveling waves from all the sources at an earlier time t. Let the source be the exact same wavefunction $\psi(x)$ at time $t < t'$, and denote the proportionality by $\mathrm{i}\mathcal{G}(x', x)$. Then we have

$$\Theta(t'-t)\psi(x') = \mathrm{i}\int \mathrm{d}^3\boldsymbol{x}\,\mathcal{G}(x',x)\,\psi(x).$$

Applying $(\mathrm{i}\partial_{t'} - \mathcal{H}(x'))$ to the above equation yields

$$(\mathrm{i}\partial_{t'} - \mathcal{H}(x'))\,(\Theta(t'-t)\psi(x')) = (\mathrm{i}\partial_{t'} - \mathcal{H}(x'))\left(\mathrm{i}\int \mathrm{d}^3\boldsymbol{x}\,\mathcal{G}(x',x)\,\psi(x)\right).$$

Since $\psi(x')$ obeys the SCHRÖDINGER equation, the left hand side is just $\mathrm{i}\delta(t'-t)\psi(x')$. This is valid for all x', so we can formally write

$$(\mathrm{i}\partial_{t'} - \mathcal{H}(x'))\,\mathcal{G}(x',x) = \delta^3(\boldsymbol{x}'-\boldsymbol{x})\delta(t'-t) \overset{\rightarrow}{=} \delta^4(x'-x),$$

with the appropriate boundary condition for outward propagation,

$$\mathcal{G}(x',x) = 0 \qquad \text{for } t' < t.$$

The computational formalism in this thesis is based on GREEN *'s functions. They describe the propagation of a particle between certain points, and this will ultimately lead us to the reflection and transmission coefficients.*
This introduction is based on the corresponding chapter in Relativistic Quantum Mechanics *by* BJORKEN *and* DRELL *, [2].*
Though later we will work with two-dimensional systems, this introduction remains in the more general three-dimensions setting.

With these boundary conditions, we have defined the retarded GREEN *'s function. In Contrast, the solution for $t < t'$ is called the advanced* GREEN *'s function, and describes anti-casual, inward traveling solutions. Unless stated otherwise, we will be concerned with retarded* GREEN *'s functions only.*

DYSON *'s equation*

Let us separate the HAMILTONIAN $\mathcal{H}$ into a free part $\mathcal{H}_0$ and an interaction V, $\mathcal{H} = \mathcal{H}_0 + V$,

$$\begin{aligned}
&(\mathrm{i}\partial_{t'} - \mathcal{H}_0(x') - V(x'))\,\mathcal{G}(x',x) = \delta^4(x'-x)\\
&(\mathrm{i}\partial_{t'} - \mathcal{H}_0(x'))\,\mathcal{G}(x',x) = \delta^4(x'-x) + V(x')\mathcal{G}(x',x)\\
&\qquad\qquad\qquad = \int \mathrm{d}^4x''\,\delta^4(x'-x'')\big(\delta^4(x''-x) + V(x'')\mathcal{G}(x'',x)\big).
\end{aligned}$$

Now we can write

$$\mathcal{G}(x',x) = \mathcal{G}_0(x',x) + \int \mathrm{d}^4x''\,\mathcal{G}_0(x',x'')V(x'')\mathcal{G}(x'',x), \tag{2.2}$$

where $\mathcal{G}_0(x',x)$ fulfills

$$(\mathrm{i}\partial_{t'} - \mathcal{H}_0(x'))\,\mathcal{G}_0(x',x) = \delta^4(x'-x).$$

This is DYSON 's equation.

Interpretation Let us write DYSON 's equation by recursively replacing the GREEN 's function on the right hand side,

$$\begin{aligned}
\mathcal{G}(x',x) =&\,\mathcal{G}_0(x',x) + \int \mathrm{d}^4x_1\,\mathcal{G}_0(x',x_1)V(x_1)\mathcal{G}_0(x_1,x)\\
&+ \iint \mathrm{d}^4x_1\,\mathrm{d}^4x_2\,\mathcal{G}_0(x',x_2)V(x_2)\mathcal{G}_0(x_2,x_1)V(x_1)\mathcal{G}_0(x_1,x) + \ldots
\end{aligned}$$

The first term describes the unperturbed propagation, the next term describes scattering at the potential $V(x_1)$ at $(\boldsymbol{x}_1, t_1)$, and the terms in the second line describe multiple scattering.

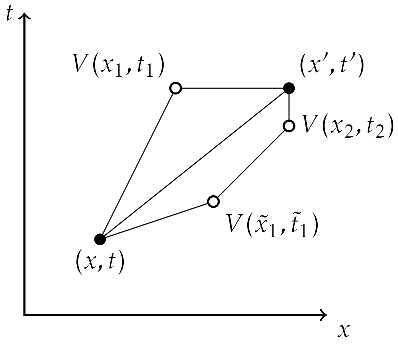

Figure 2.4: Interpretation of the DYSON *equation.*

2.5.1 *Matrix* Green*'s functions*

In numerical calculations we go from the continuum version to the discretized version of these equations. We may discretize space into a lattice of N points – the corresponding $N \times N$ (matrix) Green's function then describes the propagation between each two of these points. We will also use a tight-binding basis, where the Green's function then describes the propagation from one orbital to another one.

The equations we derived in the last subsection remain of course valid.

Recursive Green*'s function method*

This is a rather intuitive derivation of the equations of the recursive Green*'s function method. For a more formal derivation please note that the equations are simple forms of* Dyson*'s equation, Eq.* (2.2) *or see* Libisch *[18].*

In the following we describe the recursive Green's function method, which is used to obtain the Green's functions between the outermost slices of a system. One possibility to obtain this matrix is to invert $(E - \mathcal{H})^{-1} = \mathcal{G}$. However, this is inefficient for large structures. It is better to build up the structure slice by slice. In each step, we only have to remember the Green's functions between the outermost slices:

Suppose we have already calculated the Green's functions $\mathcal{G}_{11}$, $\mathcal{G}_{12}$, $\mathcal{G}_{21}$ and $\mathcal{G}_{22}$ of a block and want to attach a slice, described by $\mathcal{H}$ and the corresponding $\mathcal{G}_{33} = (E \cdot \mathbb{1} - \mathcal{H})^{-1}$, to build up the full scattering geometry step-by-step, see Fig. 2.5. The interaction Hamiltonian $\mathcal{H}_I$ between the already calculated block and the slice to attach is also known. The formulas for the Green's functions of the new block, $\tilde{\mathcal{G}}_{11}$,$\tilde{\mathcal{G}}_{13}$,$\tilde{\mathcal{G}}_{31}$ and $\tilde{\mathcal{G}}_{33}$ are intuitively understandable when one recalls that the Green's function gives the probability amplitude to travel from one position to another and is nothing but the propagator.

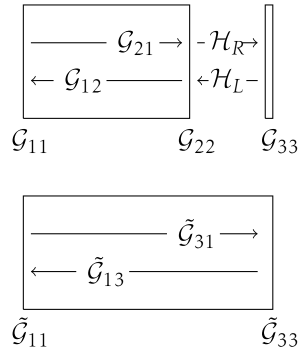

Figure 2.5: The full geometry is build up step by step.

Calculation of $\tilde{\mathcal{G}}_{33}$*:* The possible paths $\tilde{\mathcal{G}}_{33}$ which connect two positions in the new slice are those which existed before ($\mathcal{G}_{33}$) and additionally all paths which cross over to the block, interact with it and come back $\mathcal{H}_R\mathcal{G}_{22}\mathcal{H}_L$ once, twice $\mathcal{H}_R\mathcal{G}_{22}\mathcal{H}_L\mathcal{G}_{33}\mathcal{H}_R\mathcal{G}_{22}\mathcal{H}_L, \ldots$

$$\tilde{\mathcal{G}}_{33} = \mathcal{G}_{33} + \mathcal{G}_{33}\mathcal{H}_R\mathcal{G}_{22}\mathcal{H}_L\mathcal{G}_{33} + \mathcal{G}_{33}\mathcal{H}_R\mathcal{G}_{22}\mathcal{H}_L\mathcal{G}_{33}\mathcal{H}_R\mathcal{G}_{22}\mathcal{H}_L\mathcal{G}_{33} + \ldots$$

Using $(\mathbb{1} - A)^{-1} = \mathbb{1} + A + A^2 + \ldots$, this can be cast into a simpler form:

$$\begin{aligned}\tilde{\mathcal{G}}_{33} &= \mathcal{G}_{33} \cdot (\mathbb{1} - \mathcal{H}_R\mathcal{G}_{22}\mathcal{H}_L\mathcal{G}_{33})^{-1} \\ &= \left(\mathcal{G}_{33}^{-1} - \mathcal{H}_R\mathcal{G}_{22}\mathcal{H}_L\right)^{-1} \\ &= (E - \mathcal{H} - \mathcal{H}_R\mathcal{G}_{22}\mathcal{H}_L)^{-1}\end{aligned}$$

Calculation of $\tilde{\mathcal{G}}_{31}$*:* The paths from position 1 to 3 are all the paths going through the block $\mathcal{G}_{21}$, and over to the new slice, $\mathcal{G}_{33}\mathcal{H}_R$. Additionally, we have to take the paths into account which come back once, $\mathcal{G}_{33}\mathcal{H}_R\mathcal{G}_{22}\mathcal{H}_L\mathcal{G}_{33}\mathcal{H}_R$, twice, and even more often. Since we already calculated all those in $\tilde{\mathcal{G}}_{33}$, we can just write

$$\tilde{\mathcal{G}}_{31} = \tilde{\mathcal{G}}_{33}\mathcal{H}_R\mathcal{G}_{21}.$$

Calculation of $\tilde{\mathcal{G}}_{13}$: By an analogous argumentation we see that

$$\tilde{\mathcal{G}}_{13} = \mathcal{G}_{12}\mathcal{H}_L\tilde{\mathcal{G}}_{33}.$$

Calculation of $\tilde{\mathcal{G}}_{11}$: In addition to the paths which already existed ($\mathcal{G}_{11}$) there are now those which pass through the new slice, $\mathcal{H}_L\tilde{\mathcal{G}}_{33}\mathcal{H}_R$. As before, we use the new $\tilde{\mathcal{G}}_{33}$, which already contains going back and forth between the existing block and the new slice in all orders.

$$\tilde{\mathcal{G}}_{11} = \mathcal{G}_{11} + \mathcal{G}_{12}\mathcal{H}_L\tilde{\mathcal{G}}_{33}\mathcal{H}_R\mathcal{G}_{21}$$

Modular recursive Green*'s function method*

In a similar manner, we can attach a whole block to an existing block. Once a few building blocks are computed, the modular recursive Green's function method is a very efficient way to compute the Green's function of various large structures. The equations are very similar to the ones above, and are given in Section 3.4.1.

⁂

Mode basis

3

This chapter contains a complete walk-through of the calculation of reflection- and transmission coefficients in the mode basis. It is mostly based on the thesis of Sanvito *[25], with additional improvements from* Libisch *[18]. However, our derivation uses only a subset of all modes. In the relevant steps we take care to argue why this is a reasonable approximation of the exact calculation. Further, completeness in the mode basis $\sum_m |m\rangle\langle m| \neq \mathbb{1}$ does not hold. Our formulation relies on orthogonality $\langle m|m'\rangle = \delta_{mm'}$ alone.*

In Section 3.1 we motivate the use of the mode basis. Eigenfunctions of an infinite lead are calculated in Section 3.2, which are used in Section 3.3 to define the mode basis. In Section 3.4, we formulate the transport problem exclusively in blocks of a Green *'s function times an interaction* Hamiltonian *, since only combinations of $\mathcal{G}\mathcal{H}_I$ can be represented well in the mode basis.*

The reader who has an intuitive picture of modes in a confined geometry and is not interested in the technical details is invited to jump to the next chapter, Chapter 4.

3.1 *Transverse modes*

In a quantum transport experiment, electrons are usually strongly confined in all but one directions. One can use the resulting quantization to define transverse modes. The analogy with an electromagnetic waveguide is very useful here. Depending on the energy of the incoming particle, only a subset of those modes contributes to transport.

We follow the book "Electronic Transport in Mesoscopic Systems" *by* Datta *[5].*

As an example, consider a particle with parabolic dispersion in a transverse confining potential $U(y) = m\omega_0^2 y^2/2$,

We start with an effective mass equation for low-energy electrons. One can arrive at this equation from both the tight-binding model or the nearly free electron model, see e.g. [12].

$$\left(\frac{(\mathrm{i}\hbar\nabla)^2}{2m} + U(y)\right)\psi(x,y) = E\psi(x,y).$$

For ψ, we make the ansatz

$$\psi(x,y) = \frac{1}{\sqrt{L}}\mathrm{e}^{\mathrm{i}kx}\eta(y),$$

where $\eta(y)$ satisfies the equation

$$\left(\frac{\hbar^2k^2}{2m} + \frac{(\mathrm{i}\hbar\partial_y)^2}{2m} + \frac{m\omega_0^2y^2}{2m}\right)\eta(y) = E\eta(y)$$

The eigenenergies and eigenfunctions are well known and given by

$$E(n,k) = \frac{\hbar^2k^2}{2m} + \left(n+\frac{1}{2}\right)\hbar\omega_0, \qquad n = 0,1,2,\ldots$$
$$\eta_{n,k}(y) = \mathrm{e}^{-q^2/2}H_n(q), \qquad q = \sqrt{m\omega_0/\hbar}\,y,$$

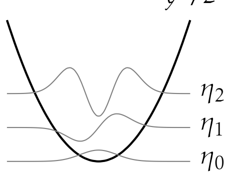

Figure 3.1: Transverse modes in a harmonic potential.

$H_n(q)$ being the n^{th} Hermite polynomial. We will refer to the states indexed by n as the different (transverse) modes. We can also read this equation in the opposite direction. For a given energy E, we can solve this equation for k. In general, there will be number of *open* or *flux-carrying modes*, for which $k \in \mathbb{R}$. As we increase n, at one point we will have $E < (n + 1/2)\hbar\omega_0$ and $k \in \mathbb{C}$, with non-vanishing imaginary part, $\operatorname{Im} k \neq 0$. We will refer to these modes as *closed* or *evanescent modes*. The solutions $\exp(ikx)\eta(y)$ with imaginary k will decay exponentially into the waveguide. Finally, let us define the energy $\epsilon_n = E(n, k = 0)$, at which the n-th mode opens, i.e. $k_n \in \mathfrak{Re} \forall E > \epsilon_n$.

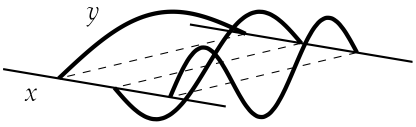

Figure 3.2: Modes in a waveguide.

3.2 *Eigenfunctions of an infinite lead*

The eigenfunctions of an infinite lead constitute the main ingredient of the mode basis. They are introduced as eigenvectors of the semi-infinite lead Hamiltonian , and their properties are discussed. We further use this section to put forward a few new methods, such as the use of shift-and-invert and blockwise inversion, which ensure an efficient calculation of the mode basis. This is of special importance, since the mode basis must be computed each time the transverse geometry changes, see Section 3.1.

In this section, we follow the thesis of Libisch *[18] and the thesis of* Sanvito *[25]*

Consider an infinite lead in x direction. Lets imagine cutting it into stripes, and let the Hamiltonian of a single stripe be $\mathcal{H}_0$. The coupling between adjacent stripes is given by $\mathcal{H}_L$ and $\mathcal{H}_R \, (= \mathcal{H}_L^\dagger)$. Then the total Hamiltonian is of the form

$$\mathcal{H} = \begin{pmatrix} \ddots & & & & \\ & \mathcal{H}_0 & \mathcal{H}_L & & \\ & \mathcal{H}_R & \mathcal{H}_0 & \mathcal{H}_L & \\ & & \mathcal{H}_R & \mathcal{H}_0 & \\ & & & & \ddots \end{pmatrix}. \tag{3.1}$$

We can solve the eigenvalue problem $\mathcal{H}\Psi = E\Psi$ with a Bloch -wave ansatz,

$$\Psi = (\ldots, \psi_{-\Delta x}, \psi_0, \psi_{\Delta x}, \ldots)^T, \qquad \psi_{\Delta x} = e^{ik\Delta x}\chi.$$

Inserting this into the eigenvalue problem yields

$$\left(\mathcal{H}_0 + e^{ik\Delta x}\mathcal{H}_L + e^{-ik\Delta x}\mathcal{H}_R\right)\chi = E\chi \tag{3.2}$$

$$\left(e^{ik\Delta x}(\mathcal{H}_0 - E) + \mathcal{H}_R\right)\chi = -e^{2ik\Delta x}\mathcal{H}_L\chi \tag{3.3}$$

This can be written as a generalized eigenvalue problem by introducing $\eta = e^{ik\Delta x}\chi$.

$$\begin{pmatrix} \mathcal{H}_0 - E & \mathcal{H}_R \\ \mathbb{1} & \end{pmatrix}\begin{pmatrix} \eta \\ \chi \end{pmatrix} = e^{ik\Delta x}\begin{pmatrix} -\mathcal{H}_L & \\ & \mathbb{1} \end{pmatrix}\begin{pmatrix} \eta \\ \chi \end{pmatrix} \tag{3.4}$$

which has $2N$ eigenvectors and $2N$ eigenvalues, N being the transverse dimension of the system. We separate the eigenvectors and eigenvalues

For example, the solutions for a simple lattice model of width L are $\chi = \sin(k_y y)$ with $k_y = n\pi/L$. The corresponding energies in the transverse directions are given by $E_t = \hbar^2 k_y^2/2m$. Whatever remains for k from the total energy goes into the factor $\exp(ik_x\Delta x)$. This means for large enough energies, or $k_x \in \mathbb{R}$, we have a few eigenvalues on the unit circle near $(1, 0)$ (for small Δx). These are the eigenvalues of propagating modes in $+k_x$ and $-k_x$. Additionally, we will find exponentially decaying modes on the real line for $k_x \in \mathbb{C}, \operatorname{Im} k_x \neq 0$.

into left-propagating (or decaying) and right-propagating (or decaying) modes according to the *group velocity*

$$\begin{aligned} v_g &= \frac{1}{\hbar}\frac{\partial E(k)}{\partial k} && (3.5)\\ &= \partial_k \langle \Psi | \mathcal{H} | \Psi \rangle && (3.6)\\ &= \mathrm{i}\Delta x \left\langle \chi \middle| \mathrm{e}^{\mathrm{i}k\Delta x}\mathcal{H}_L - \mathrm{e}^{-\mathrm{i}k\Delta x}\mathcal{H}_R \middle| \chi \right\rangle && (3.7) \end{aligned}$$

The eigenvalues of interest are located at different positions for different problems in the complex plane. For the continuum limit problem they are located around $\sigma = (1, 0)$, which can be seen by expanding $\exp(\mathrm{i}k\Delta x) \approx 1 + \mathrm{i}k\Delta x$ for small k around zero, see also Fig. 3.3. For graphene, we have to expand around the K and K' points, which are located at $K, K' = \pm 2\pi/3a$ so $\sigma = \pm\exp(\mathrm{i}2\pi/3)$. The graphene lattice parameter is denoted by a. The eigenproblem has to be solved at the K and the K' points, and the complete basis is attained by adding the two sets of eigenvectors and eigenvalues. In passing, we note that a bunch of eigenvalues lies on a closed path in the complex plane, which stays relatively close to the unit circle, see Fig. 3.4. These modes, though damped with $\exp(\mathrm{i}kl)$, still contribute to transport over small lengths l.

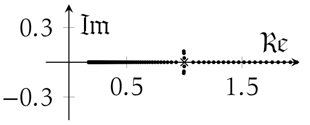

Figure 3.3: Eigenvalues of the continuum limit infinite lead in the complex plane. We highlight the point $\sigma = (1, 0)$, around which the relevant modes for transport can be found.

Shift-and-invert We now do the standard shift-and-invert transformation to the region of interest. Our eigenvalue problem is of the form

$$A\boldsymbol{x} = \lambda M\boldsymbol{x},$$

where A and M are matrices, λ are the eigenvalues and $\boldsymbol{x}$ eigenvectors of the problem. The eigenvalues of interest are located near σ. Subtracting $\sigma M\boldsymbol{x}$ from both sides yields

$$\begin{aligned} (A - \sigma M)\boldsymbol{x} &= (\lambda - \sigma)M\boldsymbol{x} && (3.8)\\ (A - \sigma M)^{-1} M\boldsymbol{x} &= \frac{1}{\lambda - \sigma}\boldsymbol{x} && (3.9)\\ \tilde{A}\boldsymbol{x} &= \nu\boldsymbol{x} && (3.10) \end{aligned}$$

a transformed eigenvalue problem. The eigenvalues of largest magnitude $|\nu|$ are exactly those nearest to σ in the original problem.

Arpack [17], a very efficient library which computes a few selected eigenvalues and vectors of large sparse matrices, is used to compute the open and “least damped” closed modes.

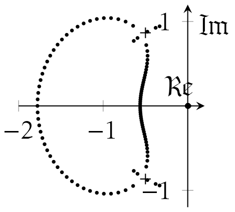

Figure 3.4: Eigenvalues of the graphene infinite lead in the complex plane. We highlight the point $\sigma = \exp(\pm\mathrm{i}2\pi/3)$, around which the relevant modes for transport can be found.

Blockwise inversion The only thing we have to do is to supply Arpack with the action of the matrix $(A - \sigma M)^{-1} M$ on a given vector. We can exploit the blockwise structure of the eigenproblem of the infinite lead Eq. (3.4) and do a part of the inversion analytically,

$$\begin{pmatrix} \mathcal{H}_0 - E + \sigma\mathcal{H}_L & \mathcal{H}_R \\ \mathbb{1} & -\mathbb{1}\sigma \end{pmatrix}^{-1} = \begin{pmatrix} (\mathcal{H}_0 - E + \sigma\mathcal{H}_L + \mathcal{H}_R/\sigma)^{-1} & (\mathcal{H}_0 - E + \sigma\mathcal{H}_L + \mathcal{H}_R/\sigma)^{-1}\mathcal{H}_R/\sigma \\ (\mathcal{H}_0 - E + \sigma\mathcal{H}_L + \mathcal{H}_R/\sigma)^{-1}\sigma & \left(\mathbb{1} + (\mathcal{H}_0 - E + \sigma\mathcal{H}_L + \mathcal{H}_R/\sigma)^{-1}\mathcal{H}_R/\sigma\right)/\sigma \end{pmatrix}$$

Note that only $(\mathcal{H}_0 - E + \sigma\mathcal{H}_L + \mathcal{H}_R/\sigma)^{-1}$ and no other inverse appear in the blocks.

With this trick, the matrix which has to be inverted is only half the size of the original problem. As in the mode basis the eigenfunctions of the infinite lead have to be computed every time the transverse geometry changes, this reduces the cost of the calculations.

3.2.1 *Sorting according to the group velocity*

We separate the eigenvectors χ into right- and leftmoving modes according to their group velocities, Eq. (3.7),

$$v_g = \mathrm{i}\Delta x \left\langle \chi \middle| \mathrm{e}^{\mathrm{i}k\Delta x}\mathcal{H}_L - \mathrm{e}^{-\mathrm{i}k\Delta x}\mathcal{H}_R \middle| \chi \right\rangle.$$

The eigenvalues of open modes, with $k \in \mathbb{R}$, lie on the unit circle, $\mathrm{e}^{\mathrm{i}k\Delta x}$. The group velocity is used to discriminate between right- ($v_g > 0$) and left moving modes ($v_g < 0$). Modes with eigenvalues inside the unit circle, $|\exp(\mathrm{i}k\Delta x)| < 1$ are evanescent right moving modes, and modes with $|\exp(\mathrm{i}k\Delta x)| > 1$ are evanescent left moving modes.

3.2.2 *Phase fixing*

In the next step, we fix the phases of the eigenvectors to avoid arbitrary phase factors in the scattering matrix between different leads. A possible way to do this is to search for the largest element in each eigenvector, and divide off its phase from the whole vector.

3.2.3 *Orthogonalization*

Since the matrix $\tilde{A}$ in Eq. (3.10) in the eigenproblem of the infinite lead is in general not hermitian, the eigenvectors will (in general) not be orthogonal. For convenience, we orthogonalize them using the (modified) GRAM-SCHMIDT process. Before we orthogonalize a new vector on the already orthogonalized set of vectors, we always check whether the new vector is linearly dependent. Checking the linear dependence is important: By orthogonalizing an (almost) linearly dependent vector, we may end up with a orthogonalized vector which corresponds to a high-frequency and exponentially increasing mode, which ultimately diminishes the numerical stability of the code. In the continuum limit case without magnetic field for example, both right- and left moving eigenvectors are identical, as can be seen from the symmetry of the problem.

It is aggravating to write this, but I urge any users of the mode basis code, (probably mostly my future self) to think of adjusting this value whenever the code gives inconsistent results. (The situation is not that bad though, all calculations in this thesis are done without adjusting this number.)

As of now, a vector is considered linear dependent if the $\mathbb{R}^N$ norm of its projection onto the already existing space is greater than a certain threshold. A more system-adapted solution, probably dependent on the system size, the type of the HAMILTONIAN and the already existing modes would be desirable.

3.3 *Definition of the mode basis*

The main building block of the mode basis are the eigenfunctions of an infinite lead obtained by periodic continuation of a single slice of grid points or atoms. Whenever the transverse dimension of the system changes, a new basis set has to be computed. Subsequently, the matrices in the mode basis are obtained via a basis transformation from the position basis.

As described up to now, the mode basis is the subset of open and weakly decaying modes of the full mode basis. This basis set however, must be enlarged. We must ensure that all matrices A which occur in the calculations leave the mode basis $\mathcal{M}$, with modes m, invariant e.g. $m' = Am$ should be in $\mathcal{M}$. Thus, the mode basis should be an invariant subspace of all matrices A. When we look at the equations, we see that matrices which occur in the calculations are the HAMILTONIAN $\mathcal{H}_0$ of a single slice, and the interaction HAMILTONIAN s $\mathcal{H}_L$ and $\mathcal{H}_R$. Additionally, there may be a potential V.

The full mode basis consists of all the N eigenvectors obtained through the eigenproblem and can be obtained by a unitary transformation of the position basis.

Separable Hamiltonian In the continuum limit problem the interaction HAMILTONIAN is a diagonal matrix $\mathcal{H}_I \propto \mathbb{1}$ and the only non-trivial matrix is the HAMILTONIAN $\mathcal{H}_0$ of a single slice. The HAMILTONIAN commutes with the interaction HAMILTONIAN , $[\mathcal{H}_0, \mathcal{H}_I] = 0$. This means the eigenvectors of the infinite lead are identical to the eigenvectors of single slice. Trivially, each single vector m of the M-dimensional mode basis spans a one-dimensional invariant subspace of all the matrices ($\mathcal{H}_0, \mathcal{H}_L$ and $\mathcal{H}_R$) which are needed to build up the scattering structure (in absence of an external potential V or varying transverse dimension). In this case, the transformation to the mode basis even stabilizes the numerical calculation.

In a more general setting, an additional x-dependent potential lifts the orthogonality between modes on adjacent slices. If the potential is weak we expect by perturbation theory only weak coupling between different modes. The modes of the unperturbed problem then still constitute a sensible basis for the problem, but now the M equations couple to one $M \times M$ dimensional problem. In addition to open modes, we can add a few closed C modes $M \to M + C$ to improve the description of tunneling phenomena as well as coupling between the open modes via the closed ones. In the low-energy regime we can discard rapidly decaying high-frequency transverse modes, we just have to add a (hopefully) few moderately damped modes. The size of the mode basis M is still small compared to the tight-binding basis N.

For the continuum limit, one can transform all matrices into the mode basis and calculate the transmission with DYSON 's equation, as given in [18]. However, when the HAMILTONIAN is non-separable, the situation is more complex, and this direct approach is numerically unstable.

Non-separable Hamiltonian/ Graphene The interaction HAMILTONIAN for graphene for example is not a diagonal matrix, and it does not commute with the HAMILTONIAN of a single slice, $[\mathcal{H}_0, \mathcal{H}_I] \neq 0$.

We have to enlarge the mode basis to describe all physical phenomena.

The implementation for graphene also includes the vectors $\mathcal{H}_0 |m\rangle$ and the largest eigenvectors of $\mathcal{H}_0$ itself. The underlying idea is that when we apply the HAMILTONIAN of a single slice to the mode basis, the resulting vectors lie in the space spanned by $\mathcal{H}_0 |m\rangle$, thus we include these vectors. Repeated application of $\mathcal{H}_0$ eventually transforms the mode basis into the largest eigenvectors of $\mathcal{H}_0$ itself.

Including the vectors $\mathcal{H}_I |m\rangle$, with $I = L$ or R, or the eigenvectors of $\mathcal{H}_I$ does not improve the results in the case of graphene. Most likely this is caused by the highly degenerate spectrum of the interaction Hamiltonian of graphene.

Mathematically,the Green 's function of a single slice, $\mathcal{G}_0 = 1/(E - \mathcal{H}_0)$ contains the Hamiltonian $\mathcal{H}_0$ in all orders, as it is $1/E + \mathcal{H}_0/E^2 + \mathcal{H}_0^2/E^3 + \ldots$. This matrix is best described by its proper eigenvectors.

The physical interpretation is that a single slice will be best represented by the eigenvalues of $\mathcal{H}_0$ itself, and the eigenvectors of a growing block will ultimately become identical to those of the infinite lead. The set $\mathcal{H}_0 |m\rangle$ ensures a gradual transition between these sets, as the operator $\mathcal{H}_0$ "pushes" the mode basis m towards its eigenvalues.

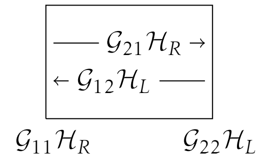
$\mathcal{G}_{21}\mathcal{H}_R \rightarrow$
$\leftarrow \mathcal{G}_{12}\mathcal{H}_L$
$\mathcal{G}_{11}\mathcal{H}_R$
$\mathcal{G}_{22}\mathcal{H}_L$

Figure 3.5: Greens *functions times interaction* Hamiltonian *of a block.*

Well behaved matrices It turns out that one needs an additional trick to make the calculation numerically stable. The invariant subspace depends not only on the modes m, but also on the matrices A which act on the modes. We observe that the Greens function of an infinite lead times the interaction Hamiltonian , $\mathcal{G}_L\mathcal{H}_L$, and $\mathcal{G}_R\mathcal{H}_R$ are diagonal in the mode basis, Eqs. (3.16) and (3.17).

Accordingly, in the limit $n_x \longrightarrow \infty$ of a very large block, the matrices $\mathcal{G}_{22}\mathcal{H}_L$, $\mathcal{G}_{12}\mathcal{H}_L$, $\mathcal{G}_{11}\mathcal{H}_R$, and $\mathcal{G}_{21}\mathcal{H}_R$ are diagonal in the mode basis. In the following section, we re-write all the Dyson equations needed to build up a scattering structure in terms of blocks of Green 's function times interaction Hamiltonian , $\mathcal{G}\mathcal{H}_I$. Then, the calculation becomes numerically stable.

3.4 *Recursive* Green *'s function method; the* Dyson *equations to add a single slice.*

We calculate the Green 's function by the recursive Green 's function method, see Section 2.5.1. The equations suitable for calculations in the mode basis are given in the following. Let us denote the leftmost slice of the existing block by 1, and the rightmost slice by 2. The Green 's function which describes the propagation from the left to the right is then called $\mathcal{G}_{21}$. The slice we want to add is denoted by 3 , see Fig. 3.6. Additionally, we need labels for the positions 0, one slice to the left of the existing block, and 4, one slice behind the new slice. Let the transverse dimension of the system at position $i = 0, 1, \ldots 4$ be n_i, and the number of modes in an infinite lead of dimension n_i be m_i.

We start by calculating the Green 's function of a single slice times the interaction Hamiltonian $\mathcal{G}\mathcal{H}_I$ in the position basis r, and transform these matrices into the mode basis m,

$$(\mathcal{G}_{33}\mathcal{H}_L)_{m,m'} = \left\langle m \middle| (E - \mathcal{H}_3)^{-1} \mathcal{H}_L \middle| m' \right\rangle$$
$$(\mathcal{G}_{33}\mathcal{H}_R)_{m,m'} = \left\langle m \middle| (E - \mathcal{H}_3)^{-1} \mathcal{H}_R \middle| m' \right\rangle$$

The indices m, m' will be omitted in the following to ensure an uncluttered notation. The matrix $\mathcal{G}_{33}\mathcal{H}_L$ is a $m_3 \times m_4$ matrix, and $\mathcal{G}_{33}\mathcal{H}_R$ has dimension $m_3 \times m_2$. In a next step, we calculate

$$I = (\mathbb{1} - \mathcal{G}_{33}\mathcal{H}_R\, \mathcal{G}_{22}\mathcal{H}_L)^{-1}\,,$$

which is a $m_3 \times m_3$ matrix. Now the updated Green 's functions times interaction Hamiltonian $\tilde{\mathcal{G}}\mathcal{H}_I$ can be computed using Dyson 's equation:

$$\begin{aligned}
\tilde{\mathcal{G}}_{33}\mathcal{H}_L &= I\, \mathcal{G}_{33}\mathcal{H}_L \\
\tilde{\mathcal{G}}_{31}\mathcal{H}_R &= I\, \mathcal{G}_{33}\mathcal{H}_R\, \mathcal{G}_{21}\mathcal{H}_L \\
\tilde{\mathcal{G}}_{11}\mathcal{H}_R &= \mathcal{G}_{11}\mathcal{H}_R + \mathcal{G}_{12}\mathcal{H}_L\, \tilde{\mathcal{G}}_{31}\mathcal{H}_R \\
\tilde{\mathcal{G}}_{13}\mathcal{H}_L &= \mathcal{G}_{13}\mathcal{H}_L\, \tilde{\mathcal{G}}_{33}\mathcal{H}_L.
\end{aligned}$$

The matrix $\tilde{\mathcal{G}}_{33}\mathcal{H}_L$ is of dimension $m_3 \times m_4$, $\tilde{\mathcal{G}}_{31}\mathcal{H}_R$ has the size $m_3 \times m_0$, $\tilde{\mathcal{G}}_{11}\mathcal{H}_R$ is a $m_1 \times m_0$ matrix, and $\tilde{\mathcal{G}}_{13}\mathcal{H}_L$ is a $m_1 \times m_4$ matrix.

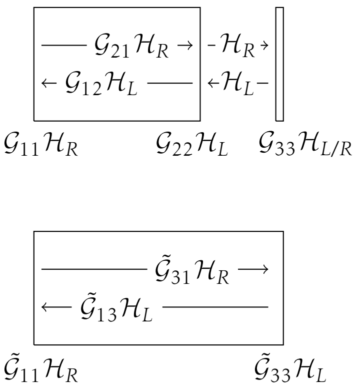

$\mathcal{G}_{21}\mathcal{H}_R$
$\mathcal{G}_{12}\mathcal{H}_L$
$\mathcal{H}_R$
$\mathcal{H}_L$
$\mathcal{G}_{11}\mathcal{H}_R$
$\mathcal{G}_{22}\mathcal{H}_L$
$\mathcal{G}_{33}\mathcal{H}_{L/R}$
$\tilde{\mathcal{G}}_{31}\mathcal{H}_R$
$\tilde{\mathcal{G}}_{13}\mathcal{H}_L$
$\tilde{\mathcal{G}}_{11}\mathcal{H}_R$
$\tilde{\mathcal{G}}_{33}\mathcal{H}_L$

Figure 3.6: The recursive Green *'s function method.*

3.4.1 *Modular recursive* Green *'s function method; the* Dyson *equations to connect two existing blocks.*

Reusing blocks reduces computational time. When we have computed a few blocks with the recursive Green 's function method, we can arbitrarily combine them into a final structure by the following Dyson equations. They combine a "left" and "right" block to a new larger block.

The leftmost slice of the left block is labeled by 1, and the rightmost slice by 2. The edges of the right block are labeled by 3 and 4. Again, we write all equations in terms of combinations of a Green 's function and an interaction Hamiltonian .

$$\begin{aligned}
\tilde{\mathcal{G}}_{12}\mathcal{H}_L &= \mathcal{G}_{12}\mathcal{H}_L\ (\mathbb{1} - \mathcal{G}_{33}\mathcal{H}_R\, \mathcal{G}_{22}\mathcal{H}_L)^{-1} \\
\tilde{\mathcal{G}}_{43}\mathcal{H}_R &= \mathcal{G}_{43}\mathcal{H}_R\ (\mathbb{1} - \mathcal{G}_{22}\mathcal{H}_L\, \mathcal{G}_{33}\mathcal{H}_R)^{-1} \\
\tilde{\mathcal{G}}_{11}\mathcal{H}_R &= \mathcal{G}_{11}\mathcal{H}_R + \tilde{\mathcal{G}}_{12}\mathcal{H}_L\, \mathcal{G}_{33}\mathcal{H}_R\, \mathcal{G}_{21}\mathcal{H}_R \\
\tilde{\mathcal{G}}_{14}\mathcal{H}_L &= \tilde{\mathcal{G}}_{12}\mathcal{H}_L\, \mathcal{G}_{34}\mathcal{H}_L \\
\tilde{\mathcal{G}}_{41}\mathcal{H}_R &= \tilde{\mathcal{G}}_{43}\mathcal{H}_R\, \mathcal{G}_{21}\mathcal{H}_R \\
\tilde{\mathcal{G}}_{44}\mathcal{H}_L &= \mathcal{G}_{44}\mathcal{H}_L + \tilde{\mathcal{G}}_{43}\mathcal{H}_R\, \mathcal{G}_{22}\mathcal{H}_L\, \mathcal{G}_{34}\mathcal{H}_L
\end{aligned}$$

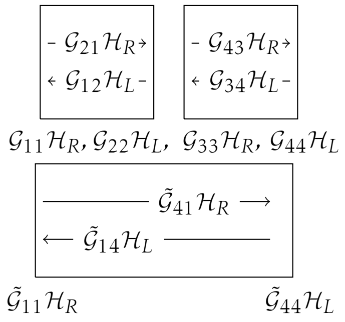

$\mathcal{G}_{21}\mathcal{H}_R$
$\mathcal{G}_{12}\mathcal{H}_L$
$\mathcal{G}_{43}\mathcal{H}_R$
$\mathcal{G}_{34}\mathcal{H}_L$
$\mathcal{G}_{11}\mathcal{H}_R, \mathcal{G}_{22}\mathcal{H}_L,\ \mathcal{G}_{33}\mathcal{H}_R, \mathcal{G}_{44}\mathcal{H}_L$
$\tilde{\mathcal{G}}_{41}\mathcal{H}_R$
$\tilde{\mathcal{G}}_{14}\mathcal{H}_L$
$\tilde{\mathcal{G}}_{11}\mathcal{H}_R$
$\tilde{\mathcal{G}}_{44}\mathcal{H}_L$

Figure 3.7: The modular recursive Green *'s function method.*

Inverse Modes Since the left- (and right-) moving eigenvectors of the infinite lead are not pairwise orthogonal, their inverse vectors $\langle l|$ (and $\langle r|$) have to be found via $\langle l|l'\rangle = \delta_{ll'}$ ($\langle r|r'\rangle = \delta_{rr'}$). In the position basis, this is done by inverting the matrix consisting of all left- (right-) moving eigenvectors. In the truncated mode basis we have to proceed differently.

Let L_r be the $n_y \times n_{\text{left moving}}$ matrix consisting of left moving eigenvectors in the position (r) basis, R_r be the $n_y \times n_{\text{right moving}}$ matrix consisting of right moving eigenvectors, and M_r be the $n_y \times n_{\text{modes}}$ matrix consisting of the mode basis vectors.

Since we have orthogonalized the mode basis, the modes L_m and R_m are (in general) not, as one would expect, diagonal matrices in the mode basis.

The states in the mode basis are given by $L_m = M_r^\dagger L_r$ and $R_m = M_r^\dagger R_r$. The inverse states are determined by $\langle l' | l \rangle = \delta_{l'l}$, and $\langle r' | r \rangle = \delta_{r'r}$ They may be obtained by computing

$$L' = L\left(A^{-1}\right)^\dagger, \qquad R' = R\left(\tilde{A}^{-1}\right)^\dagger, \tag{3.11}$$

In practical calculations we have to be careful to use the same set of inverse vectors for the whole calculation (lead, transmission) and not to mix different calculations

where

$$A = L^\dagger L, \qquad \tilde{A} = R^\dagger R$$

since now $L'^\dagger L \overset{\rightarrow}{=} A^{-1} L^\dagger L = \mathbb{1}$, and analogously $R'^\dagger R = \mathbb{1}$. The dimensions of L (and L', R, R') is $n_y \times n_B$, where n_y is the transverse dimension of the lead, and n_B is the number of left- (and right-) moving basis vectors. There is thus a freedom in the choice of the inverse vectors $|l\rangle'$ and $|r\rangle'$. .

Greens function for a half-infinite lead

This derivation can be found in SANVITO *'s thesis [25] and was simplified by* LIBISCH *, [18].*

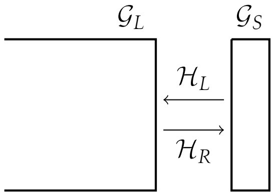

Figure 3.8: Derivation of the surface GREEN *'s function $\mathcal{G}_L$ of a semi-infinite lead. The* GREEN *'s function of a single slice is given by $\mathcal{G}_S$.*

We calculate the surface GREEN 's function $\mathcal{G}_L$ of a semi-infinite lead by making use of the DYSON equation, Eq. (2.2). Our "unperturbed" GREEN 's function $\mathcal{G}_0$ is the GREEN 's function of a single slice $\mathcal{G}_S$. The "perturbation" V is the coupling $\mathcal{H}_R \mathcal{G}_L \mathcal{H}_L$ to an already existing half infinite lead $\mathcal{G}_L$. After we attach the slice, the total GREEN 's function is still the GREEN 's function of a half infinite lead, $\mathcal{G}_L$.

$$\mathcal{G}_L = \mathcal{G}_S + \mathcal{G}_S \mathcal{H}_R \mathcal{G}_L \mathcal{H}_L \mathcal{G}_L \tag{3.12}$$

$$(E - \mathcal{H}_0)\mathcal{G}_L \mathcal{H}_L = \mathcal{H}_L + \mathcal{H}_R \left(\mathcal{G}_L \mathcal{H}_L\right)^2 \tag{3.13}$$

$$(E - \mathcal{H}_0) \textstyle\sum_i |\xi_i\rangle\, 1/\beta_i \,\langle \xi_i| = \mathcal{H}_L + \mathcal{H}_R \sum_i |\xi_i\rangle\, 1/\beta_i^2 \,\langle \xi_i| \tag{3.14}$$

$$(\beta(\mathcal{H}_0 - E) + \mathcal{H}_R)|\xi\rangle = -\beta^2 \mathcal{H}_L |\xi\rangle \tag{3.15}$$

The eigenvectors $\langle \xi_i |$ are defined via $\langle \xi_j | \xi_i \rangle = \delta_{ij}$, see also Eq. (3.11).

In the second line, we use the definition of the GREEN 's function $\mathcal{G}_S = 1/(E - \mathcal{H}_0)$ and further right-multiply with $\mathcal{H}_L$. In the third line, we write $\mathcal{G}_L \mathcal{H}_L$ as an eigenvalue expansion $\mathcal{G}_L \mathcal{H}_L = |\xi_i\rangle\, 1/\beta_i \,\langle \xi_i|$. By comparison with the eigenvalue equation for an infinite lead, Eq. (3.2), we see that the eigenfunctions of the semi-infinite lead are the same as those for an infinite lead. The physical boundary conditions restrict us to the N eigenvalues of unit magnitude or the exponentially decaying eigenvalues corresponding to the left-moving eigenstates $|l\rangle$, and not the exponentially increasing right-moving eigenvalues. Thus we can write

$$\mathcal{G}_L \mathcal{H}_L = \sum_l |l\rangle\, \mathrm{e}^{\mathrm{i}k_l \Delta x} \,\langle l|. \tag{3.16}$$

In the calculation of the semi-infite lead extending to the right $\mathcal{G}_R$, the matrices $\mathcal{H}_L \leftrightarrow \mathcal{H}_R$ swap place compared to the calculation for $\mathcal{G}_L$ (see Eq. (3.15)). This results in one over the eigenvalues $1/\beta \leftrightarrow \beta$ being replaced by the actual eigenvalues β and one obtains

$$\mathcal{G}_R \mathcal{H}_R = \sum_r |r\rangle\, \mathrm{e}^{-\mathrm{i}k_r \Delta x} \,\langle r|, \tag{3.17}$$

where $|r\rangle$ are the right-moving eigenstates and $e^{-ik_r\Delta x}$ the eigenvalues.

Let us note that each eigenvalue weights the outer product of the corresponding eigenvectors in importance. The magnitude of the eigenvalues of low-energy modes, where $k \in \mathbb{R}$, is 1. High frequency modes, with $\mathrm{Im}(k) >> \Delta x$ are damped exponentially and can be omitted in practice.

3.4.2 *Attaching the leads*

For the calculation of the Green 's function of the system including the right lead, we insert an additional slice between structure and lead, and calculate its interaction to both sides.

$$I = (\mathbb{1} - \mathcal{G}_{33}\mathcal{H}_R\,\mathcal{G}_{22}\mathcal{H}_L - \mathcal{G}_{33}\mathcal{H}_L\,\mathcal{G}_R\mathcal{H}_R)^{-1},$$

which is a $m_3 \times m_3$ matrix. Now the updated Green 's functions $\tilde{\mathcal{G}}$ can again be computed using Dyson 's equation:

$$\begin{aligned}
\tilde{\mathcal{G}}_{33}\mathcal{H}_L &= I\,\mathcal{G}_{33}\mathcal{H}_L \\
\tilde{\mathcal{G}}_{31}\mathcal{H}_R &= I\,\mathcal{G}_{33}\mathcal{H}_R\,\mathcal{G}_{21}\mathcal{H}_L \\
\tilde{\mathcal{G}}_{11}\mathcal{H}_R &= \mathcal{G}_{11}\mathcal{H}_R + \mathcal{G}_{12}\mathcal{H}_L\,\tilde{\mathcal{G}}_{31}\mathcal{H}_R \\
\tilde{\mathcal{G}}_{13}\mathcal{H}_L &= \mathcal{G}_{13}\mathcal{H}_L\,\tilde{\mathcal{G}}_{33}\mathcal{H}_L.
\end{aligned}$$

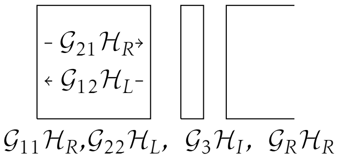
- $\mathcal{G}_{21}\mathcal{H}_R$→
← $\mathcal{G}_{12}\mathcal{H}_L$-
$\mathcal{G}_{11}\mathcal{H}_R$,$\mathcal{G}_{22}\mathcal{H}_L$,
$\mathcal{G}_3\mathcal{H}_I$,
$\mathcal{G}_R\mathcal{H}_R$

Figure 3.9: Attaching the right lead.

The equations for the left lead are similar. This time we insert the slice 0 between the left lead L and the structure.

$$I = (\mathbb{1} - \mathcal{G}_{00}\mathcal{H}_L\,\mathcal{G}_{11}\mathcal{H}_R - \mathcal{G}_{00}\mathcal{H}_R\,\mathcal{G}_L\mathcal{H}_L)^{-1},$$

which is a $m_3 \times m_3$ matrix. The updated Green 's functions $\tilde{\mathcal{G}}$ read

$$\begin{aligned}
\tilde{\mathcal{G}}_{00}\mathcal{H}_R &= I\,\mathcal{G}_{00}\mathcal{H}_R \\
\tilde{\mathcal{G}}_{02}\mathcal{H}_L &= I\,\mathcal{G}_{00}\mathcal{H}_L\,\mathcal{G}_{12}\mathcal{H}_L \\
\tilde{\mathcal{G}}_{22}\mathcal{H}_L &= \mathcal{G}_{22}\mathcal{H}_L + \mathcal{G}_{21}\mathcal{H}_R\,\tilde{\mathcal{G}}_{02}\mathcal{H}_L \\
\tilde{\mathcal{G}}_{21}\mathcal{H}_R &= \mathcal{G}_{21}\mathcal{H}_R\,\tilde{\mathcal{G}}_{00}\mathcal{H}_R.
\end{aligned}$$

Transmission

Consider an infinite lead, where the lead Green 's function $\mathcal{G}_L$ fulfills

$$(E - \mathcal{H}_L)\mathcal{G}_L = \mathbb{1},$$

and the lead wavefunction ψ_L fulfills

$$(E - \mathcal{H}_L)\psi_L = 0.$$

Let us replace a part of the lead by the scattering structure and denote by $\mathcal{H}_S$ the difference of the Hamiltonian of the scattering structure and the Hamiltonian of the infinite lead. The total Green 's function $\mathcal{G}$ and the wavefunction ψ now fulfill

$$(E - \mathcal{H}_L - \mathcal{H}_S)\mathcal{G} = \mathbb{1}$$

We are still following Sanvito *'s thesis [25], though we depart in the end.* Sanvito *'s method requires the introduction of an operator (the matrix $\mathcal{V}$ in Eq. 2.30 in his thesis) which is not accessible in the mode basis. We show that transmission and reflection coefficients can be extracted even in the (non-complete) mode basis.*

and

$$(E - \mathcal{H}_L - \mathcal{H}_S)\psi = 0.$$

Dyson's equation relates the two Green's functions,

$$\mathcal{G} = (\mathbb{1} - \mathcal{G}_L \mathcal{H}_S)^{-1}\, \mathcal{G}_L,$$

and accordingly the wavefunctions

$$\psi = (\mathbb{1} - \mathcal{G}_L \mathcal{H}_S)^{-1}\, \psi_L.$$

In the following, we want to find a vector $|p\rangle$ which projects the wavefunction out of the Green's function of an infinite lead, $\mathcal{G}_L\,|p\rangle = |\psi_L\rangle$. Then we can show that the same vector projects the total wavefunction $|\psi\rangle$ out of the total Green's function $\mathcal{G}$,

$$\begin{aligned}|\psi\rangle &= (\mathbb{1} - \mathcal{G}_L \mathcal{H}_S)^{-1}\, |\psi_L\rangle \\ &= (\mathbb{1} - \mathcal{G}_L \mathcal{H}_S)^{-1}\, \mathcal{G}_L\,|p\rangle \\ &= \mathcal{G}\,|p\rangle.\end{aligned}$$

To proceed, we write the Green's function between the points z and z' in the form

$$\mathcal{G}_{zz'} = \begin{cases} \sum_r |r\rangle \mathrm{e}^{\mathrm{i}k_r(z-z')} \langle a_r|, & z \geq z' \\ \sum_l |l\rangle \mathrm{e}^{\mathrm{i}k_l(z-z')} \langle a_l|, & z \leq z'. \end{cases}$$

The sum runs over all right- (r) or leftmoving (l) eigenvalues and -vectors, and $|a_r\rangle$ and $|a_l\rangle$ are still to determine. When acted on with the projection vector $|p\rangle$, it gives a superposition of right and left moving plane waves. Inserting this into the defining equation, $(E - \mathcal{H})\mathcal{G} = \mathbb{1}$ gives, together with the Hamiltonian of an infinite lead (Eq. (3.1)), the equation

$$(E - \mathcal{H}_0)\sum_r |r\rangle\langle a_r| - \mathcal{H}_L \sum_r |r\rangle \mathrm{e}^{\mathrm{i}k_r\Delta x} \langle a_r| - \mathcal{H}_R \sum_l |l\rangle \mathrm{e}^{-\mathrm{i}k_l\Delta x} \langle a_l| = \mathbb{1}.$$

Using Eq. (3.2) from the infinite lead yields

$$\mathcal{H}_R \left(\sum_r |r\rangle \mathrm{e}^{-\mathrm{i}k_r\Delta x} \langle a_r| - \sum_l |l\rangle \mathrm{e}^{-\mathrm{i}k_l\Delta x} \langle a_l| \right) = \mathbb{1}.$$

The Green's function has to be continuous at $z = z'$, so $\sum_r |r\rangle\langle a_r| = \sum_l |l\rangle\langle a_l|$. Left multiplying with $\langle r'|$, where $\langle r'|r\rangle = \delta_{rr'}$ yields $\langle a_{r'}| = \sum_l \langle r'|l\rangle\langle a_l|$. Then we have

$$\begin{gathered}\mathcal{H}_R \left(\sum_r |r\rangle \mathrm{e}^{-\mathrm{i}k_r\Delta x} \sum_l \langle r|l\rangle\langle a_l| - \sum_l |l\rangle \mathrm{e}^{-\mathrm{i}k_l\Delta x} \langle a_l| \right) = \mathbb{1} \\ \mathcal{H}_R \left(\sum_r |r\rangle \mathrm{e}^{-\mathrm{i}k_r\Delta x} \langle r| - \sum_l |l\rangle \mathrm{e}^{-\mathrm{i}k_l\Delta x} \langle l| \right) \sum_{l'} |l'\rangle\langle a_{l'}| = \mathbb{1},\end{gathered}$$

where $\langle l'|l\rangle = \delta_{ll'}$. We have computed the vector $|a_{l'}\rangle$, which is defined by $\langle a_{l'}|a_l\rangle = \delta_{ll'}$,

$$|a_{l'}\rangle = \mathcal{H}_R \left(\sum_r |r\rangle \mathrm{e}^{-\mathrm{i}k_r\Delta x} \langle r| - \sum_l |l\rangle \mathrm{e}^{-\mathrm{i}k_l\Delta x} \langle l| \right) |l'\rangle .$$

Analogously, we find

$$|a_{r'}\rangle = \mathcal{H}_R \left(\sum_r |r\rangle \mathrm{e}^{-\mathrm{i}k_r\Delta x} \langle r| - \sum_l |l\rangle \mathrm{e}^{-\mathrm{i}k_l\Delta x} \langle l| \right) |r'\rangle ,$$

where $\langle a_{r'}|a_r\rangle = \delta_{rr'}$.

The projector $|p\rangle$ we set out for is, for $z \geq z'$, just

$$|p_r(z)\rangle = |a_r\rangle \mathrm{e}^{\mathrm{i}k_r z'} / \sqrt{v_r},$$

since acting with it on the Green 's function $\mathcal{G}_{zz'} = \sum_{r'} |r'\rangle \mathrm{e}^{\mathrm{i}k_{r'}(z-z')} \langle a_{r'}|$ yields the normalized plane wave $|\psi\rangle = |r\rangle \frac{\mathrm{e}^{\mathrm{i}k_r z}}{\sqrt{v_r}}$.

We are assuming distinct k values. For the degenerate case, please refer to Sanvito *'s thesis[25].*

We also know the form of the left side of the equation $|\psi\rangle = \mathcal{G}|p\rangle$, namely

$$|\psi_z\rangle = \begin{cases} \frac{\mathrm{e}^{\mathrm{i}k_r z}}{\sqrt{v_r}} |r\rangle + \sum_l \frac{r_{lr}}{\sqrt{-v_l}} \mathrm{e}^{\mathrm{i}k_l z} |l\rangle & z \leq 0 \\ \sum_{r''} \frac{t_{r''r}}{\sqrt{v_{r''}}} \mathrm{e}^{\mathrm{i}k_{r''} z} |r''\rangle & z \geq 0, \end{cases}$$

where r_{lr} is the reflection coefficient from the incoming right-moving mode r into the outgoing left-moving mode l and $t_{r''r}$ is the transmission coefficient from the incoming right-moving mode r into the outgoing right-moving mode r''. Finally we can extract the reflection and transmission coefficients. We use the numerically computed G in $|\psi\rangle = \mathcal{G}|p\rangle$, and act on it with $\langle r'|$ to obtain, for $z \geq 0$, the transmission

$$t_{r'r} = \langle r'| \mathrm{e}^{-\mathrm{i}k_{r'}(z_2-z_1)} \frac{\sqrt{v_{r'}}}{\sqrt{v_r}} \mathcal{G}_{21} \mathcal{H}_R \left(\sum_{r''} |r''\rangle \mathrm{e}^{-\mathrm{i}k_{r''}\Delta x} \langle r''| - \sum_l |l\rangle \mathrm{e}^{-\mathrm{i}k_l\Delta x} \langle l| \right) |r\rangle . \tag{3.18}$$

At $z = 0$, we can extract the reflection

$$r_{lr} = \langle l| \frac{\sqrt{-v_l}}{\sqrt{v_r}} \left(\mathcal{G}_{11} \mathcal{H}_R \left(\sum_{r''} |r''\rangle \mathrm{e}^{-\mathrm{i}k_{r''}\Delta x} \langle r''| - \sum_l |l\rangle \mathrm{e}^{-\mathrm{i}k_l\Delta x} \langle l| \right) - \mathbb{1} \right) |r\rangle . \tag{3.19}$$

If we sum over all modes, these equations are identical to those given in Sanvito 's thesis[25].

In contrast this derivation shows that summing over all possible modes is not necessary. The mistake we make by neglecting evanescent modes is, as can be seen by checking the terms in Eq. (3.18) and Eq. (3.19), only exponentially small.

⁂

Computations in the Mode basis

4

In Section 4.1, we hint at the gains in efficiency which can be obtained with the mode basis. We calculate the scattering matrix of simple building blocks of more complicated geometries in Section 4.2. Resonances and their effect on the mode basis approximation are discussed in Section 4.3. The mode basis can be used for moderate magnetic fields, see Section 4.4.

4.1 Timing

The main reason to do the transformation into the mode basis is the gain in efficiency. To get a feeling for the speed of the algorithm, we measure the time needed to compute the transmission of a quadratic graphene flake at fixed energy for various system sizes. The tests are done on a notebook with an Intel Core i7 processor. Both calculations are done on a single core and both use the recursive GREEN's function method. Of course, further gains in efficiency are easily possible by using the modular recursive GREEN's function method and parallel computing. But since the recursive GREEN's function method on a single core is the building block of all further methods, our test still has its validity.

At $E = 0.1\,\mathrm{eV}$, the mode basis is able to calculate structures which are an order of magnitude larger than the position basis, see Fig. 4.1. The gains in computational speed are a direct result of the smaller matrix sizes in the mode basis. A fit gives a computational time

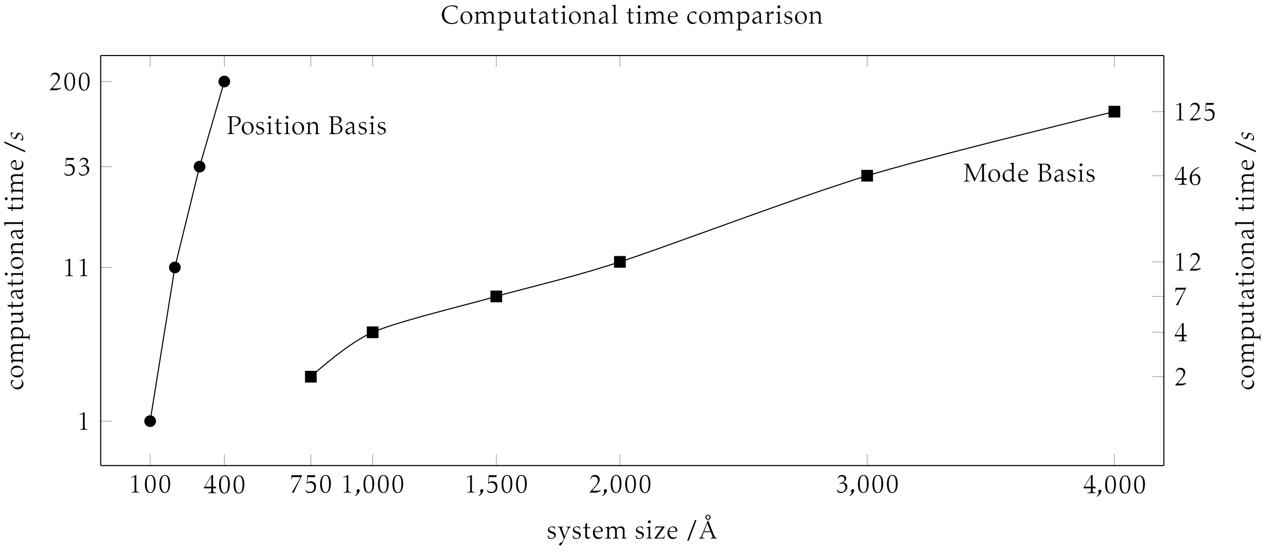

Figure 4.1: Computational time comparison between the recursive GREEN*'s function method in position basis and in the mode basis. The system is a quadratic graphene flake and the transmission is computed at* $E = 0.1\,\mathrm{eV}$

t dependence on the system size n of about $\mathcal{O}(n^{3.9})$ for the exact calculation and $\mathcal{O}(n^{3.8})$ for the mode basis. Matrix multiplications, which go with $\mathcal{O}(n^3)$ constitute a lower bound for all calculations.

Due to the large number of modes at $E = 1\,\text{eV}$ (141 open and 386 in total for a size of 1000 Å) the situation changes. Using the mode basis, we can only calculate a system twice as large as in the position basis in the same time (compare the two curves in Fig. 4.2). This does not come as a surprise, as with 386 modes we are in the range of the exact system with $n_y = 400$ atomic orbitals.

Why do we need so many modes? As explained in Section 3.3, the full modebasis consists of right- and left moving open modes, as well as closed modes. Further we include the eigenvectors of the Hamiltonian of a single slice as well as the action of a single slice on the mode basis.

One might wonder why the calculation with matrices of size 386 in the mode basis is slower than the exact calculation with matrices of size 400. This is due to the fact that we need to solve three eigenproblems (see the paragraph above) and that we have to do a few basis transformations between the orbital basis ($N = 1000$) and the mode basis ($M = 386$). These matrices are of size 1000×386.

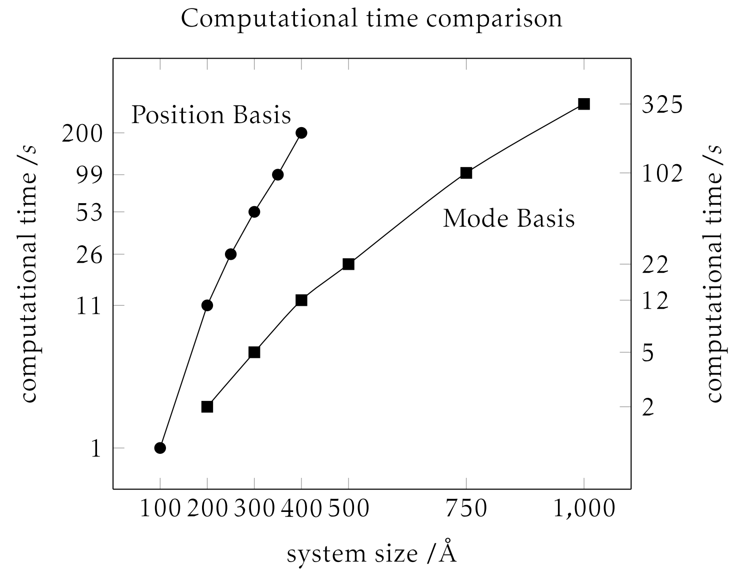

Figure 4.2: Computational time comparison between the recursive Green *'s function method in position basis and in the mode basis. The system is a quadratic graphene flake and the transmission is computed at* $E = 1\,\text{eV}$.

In contrast, when we decrease the energy with increasing system size, and thereby keep the number of propagating modes constant, the computational time in the mode basis is much smaller.

We further remark that the relevant energy region for graphene-transport calculations is near the Fermi energy and thus well below $E = 1\,\text{eV}$.

4.2 *Building Blocks*

In this section we investigate how well calculations using the (truncated) mode basis perform for various geometries. We give

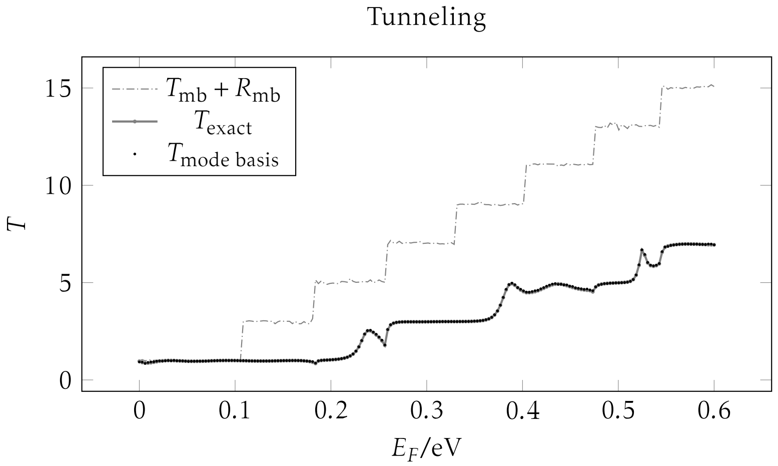

Figure 4.3: Transmission through a graphene scattering structure. The mode basis calculation (black dots) lies on top of the exact calculation (gray line). Transmission plus reflection (dashed line) add up to the number of open modes. Dimensions: Leads: $W = 20\,\mathrm{nm}$, *structure:* $W = 10\,\mathrm{nm}$, $L = 10\,\mathrm{nm}$. *The leads are described by 66 modes instead of 204 tight binding orbitals, and the scattering region by 48 modes instead of 100 orbitals. Parameters in the calculation: 50 eigenvalues, 16 left and 16 right moving modes, 10 eigenfunctions of* $\mathcal{H}_0$ *for the* 10 nm, *and 90 eigenvalues, 30 left and 30 right moving modes, 12 eigenfunctions of* $\mathcal{H}_0$ *for the* 20 nm.

examples of various simple "building blocks" like a constriction or a cavity, of a more complex scattering structure.

Tunneling The first geometry we want to test is a 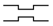 constriction. Physically, the reflection originates from the position where the transverse size decreases. Once the particle is inside the small region, it can enter the wide region almost reflectionless. Resonances of the small region couple strongly to the wide leads and are therefore very broad and much less important than in a cavity.

The mode basis describes the physics astonishingly well (see Fig. 4.3), though only the subset of low frequency modes is used. Transmission plus reflection should equal exactly the number of incoming open modes. As the transformation into the truncated mode basis is an approximation, slight inaccuracies at certain points don't come unexpected.

Cavity The next geometry we consider at is a cavity, 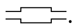. The width of the cavity is twice the width of the leads. The current can enter the cavity almost reflectionless, but scatters multiple times before it leaves the cavity at either side. This results in a complicated transmission curve (Fig. 4.4). The mode basis again reproduces the exact calculation in great detail, with the exception of small regions. Around these points however, the vulnerability of the approach becomes apparent. In these cases, the unitarity (reflection and transmission should equal the number of open modes) provides a consistency check.

Dependence of the numerical stability in the number of modes We want to discuss how many modes we have to include in the calculations.

When we include as many modes as we have tight-binding orbitals, we have a unitary transformation into the mode basis and the calculation is exact. The other extreme would be to solely include open modes. This however, works only for a featureless waveguide without any additional potential or changes in the transverse dimension. The

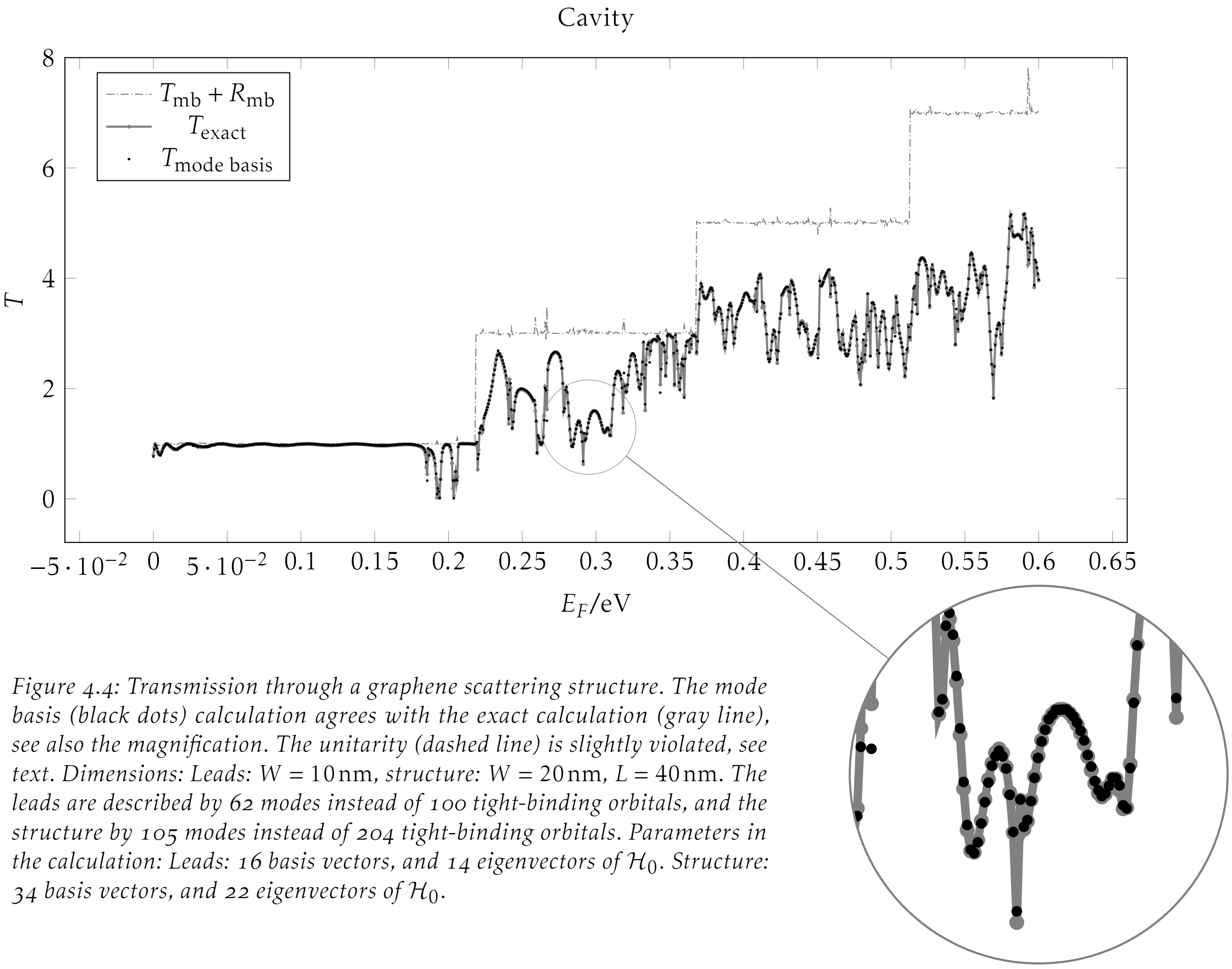

Figure 4.4: Transmission through a graphene scattering structure. The mode basis (black dots) calculation agrees with the exact calculation (gray line), see also the magnification. The unitarity (dashed line) is slightly violated, see text. Dimensions: Leads: $W = 10\,\mathrm{nm}$, *structure:* $W = 20\,\mathrm{nm}$, $L = 40\,\mathrm{nm}$. *The leads are described by 62 modes instead of 100 tight-binding orbitals, and the structure by 105 modes instead of 204 tight-binding orbitals. Parameters in the calculation: Leads: 16 basis vectors, and 14 eigenvectors of* $\mathcal{H}_0$. *Structure: 34 basis vectors, and 22 eigenvectors of* $\mathcal{H}_0$.

accurate description of non-trivial cases requires higher frequency modes. But how many modes do we have to include? The more complicated the structure is, the more modes we have to include, as can be seen from the constriction in Fig. 4.3 and the cavity (Fig. 4.4, calculation with the same number of modes not shown). Though both structures consist of a wide (66 modes/204 tight binding orbitals) and a small (48 modes/100 orbitals) region, the simpler constriction shows perfect agreement with the exact calculation whereas the cavity already deviates strongly at certain points.

Why do we still have so many modes? For graphene, we need a few evanescent modes to stabilize the calculation. Let us say we have 5 open modes, and roughly ten closed modes. Multiply by two to describe both left- and right moving states, and we are at 30 modes. As discussed in Section 3.3, we also have to include $\mathcal{H}_0 |m\rangle$, *which gives 60. Finally, we have to add a few eigenfunctions of* $\mathcal{H}_0$. *We now have a minimum of 70 modes, though this number is still reduced by possible linear dependences. With increasing system size, we generally need to increase the number of modes. The ratio between system size and number of modes however becomes better.*

Let us investigate the cavity more closely. Starting directly with Fig. 4.4, 62 modes instead of 100 tight-binding orbitals for the leads and 105 modes instead of 204 tight-binding orbitals describe the cavity very well. Successively decreasing the number of modes used in the calculation (see Figs. 4.5 and 4.6) makes the calculation more and more unstable.

Hence, no general answer on how many modes have to be included can be given. The figures in this chapter can provide a rough guideline.

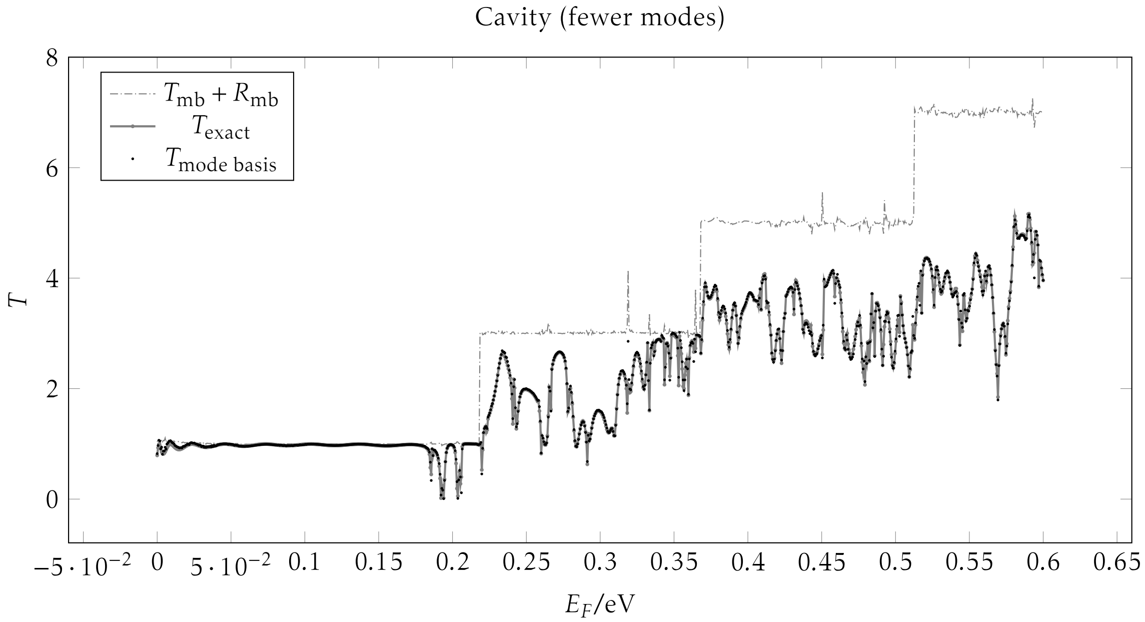

Figure 4.5: Transmission through a graphene scattering structure. The mode basis (black dots) calculation agrees with the exact calculation (gray line). Since fewer modes are used, the unitarity (dashed line) is slightly violated, see text. Dimensions: Leads: $W = 10\,\text{nm}$, *structure:* $W = 20\,\text{nm}$, $L = 40\,\text{nm}$. *The leads are described by 53 modes instead of 100 tight-binding orbitals, and the structure by 79 modes instead of 204 tight-binding orbitals. Parameters in the calculation: Leads: 14 basis vectors, and 10 eigenvectors of* $\mathcal{H}_0$. *Structure: 22 basis vectors, and 16 eigenvectors of* $\mathcal{H}_0$.

For more complex situations, we suggest to look for unitarity violations ($T + R = N_{\text{modes}}$) of the mode basis especially near sharp resonances and increase the number of modes accordingly.

Two Cavities We observe that the calculation of two connected cavities of width 20 nm and length 40 nm, 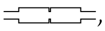, where the constriction is 1 nm long and 10 nm wide is still stable, see Fig. 4.7. With this extremely short constriction we want to test cases where tunneling through evanescent modes becomes important.

The stability of the calculation in the mode basis is not guaranteed. At close inspection it can be seen that the agreement with the exact calculation is not as good as for the single cavity, Fig. 4.4.

Ferry et al. describe the mode matching technique in their book *Transport in Nanostructures*[7]. One "breaks up a geometry into sections and expands stationary-state solutions in transverse modes characterizing a particular section". Then one matches the solution and its derivatives across the boundary of different sections. This procedure may cause numerical instabilities due to exponentially growing modes. Our mode basis approach is conceptually close to this mode matching technique, so we should be aware of a possible breakdown for complicated geometries.

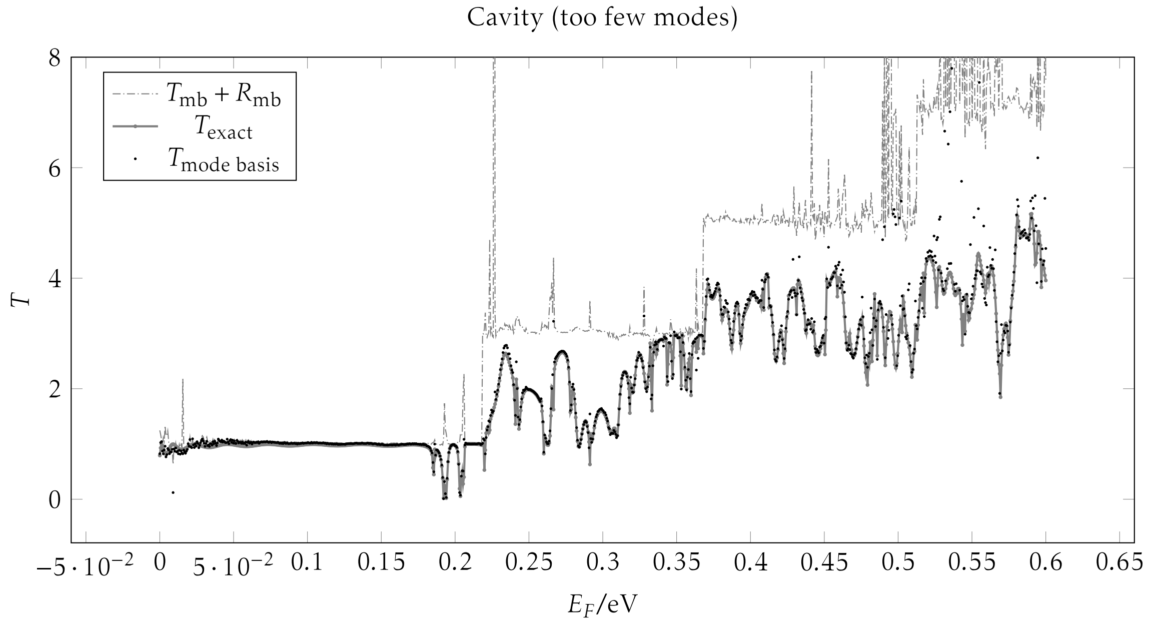

Figure 4.6: Transmission through a graphene scattering structure using too few modes. The mode basis (black dots) calculation fails to reproduce the exact calculation (gray line). The unitarity (dashed line) is heavily violated, see text. Dimensions: Leads: $W = 10\,\text{nm}$, *structure:* $W = 20\,\text{nm}$, $L = 40\,\text{nm}$. *The leads are described by 41 modes instead of 100 tight-binding orbitals, and the structure by 62 modes instead of 204 tight-binding orbitals. Parameters in the calculation: Leads: 10 basis vectors, and 6 eigenvectors of* $\mathcal{H}_0$. *Structure: 16 basis vectors, and 10 eigenvectors of* $\mathcal{H}_0$.

4.3 Resonances

For an introduction to Fano *resonances, please see Section 2.2.*

At various points in the transmission curve, resonances which are both asymmetric and very sharp can be observed. One of them appears in the region around $E = 0.2656\,\text{eV}$ in the cavity of length $L = 40\,\text{nm}$ and width $W = 20\,\text{nm}$, see Figs. 4.4 to 4.6. For closer inspection, the calculation is redone with a tighter spacing in this energy window, see Fig. 4.8. The characteristic Fano line shape suggests that an interference effect between the continuum states in the leads and an eigenstate of the cavity takes place. Since the width of the peak is determined by its imaginary part, we conclude that this state couples only weakly to the leads. We search for eigenstates of the (closed) cavity at this energy and indeed find a state at $E = 0.2648\,\text{eV}$ which resembles the scattering state at $E = 0.2656\,\text{eV}$ closely (not shown). As violations in the unitarity are always accompanied by a characteristic sharp and asymmetric line shape in the transmission curve, we conclude that resonant scattering on states with a long lifetime induces these numerical instabilities. Why is the description of these states challenging? These states traverse the structure many times, or put differently, reflect multiple times at the constrictions. Small errors which are inevitable introduced in the mode basis approximation are amplified.

Future work could be dedicated to an accurate description of these resonances in the mode basis. A possible approach would be to

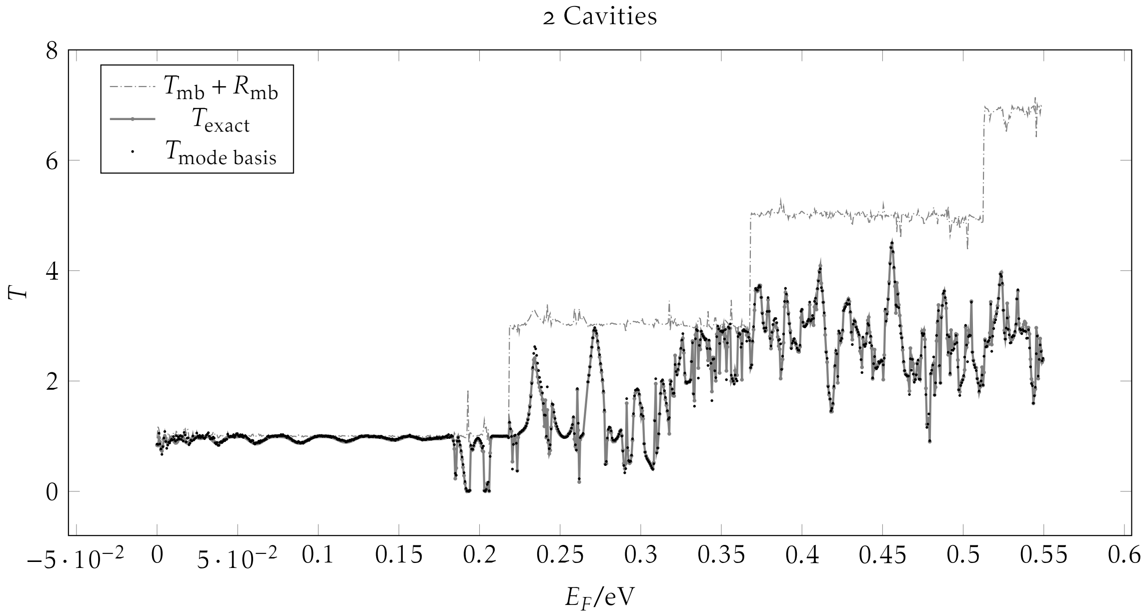

Figure 4.7: Transmission through a graphene scattering structure. The mode basis (black dots) calculation agrees with the exact calculation (gray line). The unitarity (dashed line) is slightly violated, see text. Dimensions: Leads: $W = 10\,\mathrm{nm}$, *structure:* $W = 20\,\mathrm{nm}$, $L = 40\,\mathrm{nm}$, *followed by* $W = 10\,\mathrm{nm}$, $L = 2\,\mathrm{nm}$ *and then again* $W = 20\,\mathrm{nm}$, $L = 40\,\mathrm{nm}$. *The leads are described by 48 modes instead of 100 tight binding orbitals, and the scattering region by 66 modes instead of 204 orbitals. Parameters in the calculation: 50 eigenvalues, 16 left and 16 right moving modes, 14 eigenfunctions of* $\mathcal{H}_0$ *for the* $10\,\mathrm{nm}$, *and 102 eigenvalues, 34 left and 34 right moving modes, 22 eigenfunctions of* $\mathcal{H}_0$ *for the* $20\,\mathrm{nm}$.

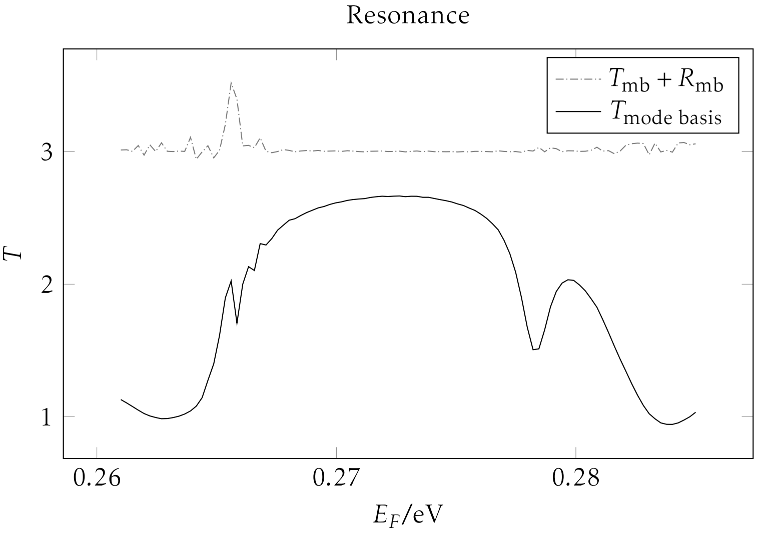

Figure 4.8: Resonance in the transmission curve. This is the same cavity and data as in Fig. 4.4, but we now focus on the region around $E = 0.2656\,\mathrm{eV}$, *where the unitarity* ($T_{mb} + R_{mb}$, *dashed line) is violated in the mode basis. This can be attributed to an eigenstate of the cavity at* $E = 0.2648\,\mathrm{eV}$, *see text. Compare also this line shape with the coupled oscillator model, Fig. 2.2*

include the projection of the eigenstate on the current slice into the mode basis.

This argument has to be taken with a grain of salt, since it is not valid for complex scattering structures, see [23].

Discrepancy in Transmission and Reflection The error in the reflection coefficient is generally larger than in the transmission coefficient (see especially Fig. 4.5). A possible explanation is that the computation of the reflection has, for a nearly ballistic device, more chance to err than the computation of the transmission. Intuitively, one has to go through the structure once to compute the transmission, but one has to go back again to compute the reflection. Mathematically, twice as many matrix multiplications are used for the computation of the GREEN 's function $\mathcal{G}_{11}$, which ultimately determines the reflection, as are used for $\mathcal{G}_{21}$, which determines the transmission, see Chapter 3. A second possible explanation is that while the GREEN 's function $\mathcal{G}_{21}$ is almost diagonal in the right-moving modes, the GREEN 's function $\mathcal{G}_{11}$ has components of both right- and left moving modes. At the moment the mode basis code orthogonalizes all right moving modes first, and then all left moving modes. Thus more errors are introduced into the left moving part, since the orthogonalized mode may now overlap with exponentially increasing modes. The apparent solution is to orthogonalize all open (and thus important) modes first, and the closed modes afterwards. Since this is an obvious flaw in the current implementation, the discrepancy in errors between transmission and reflection coefficients is not investigated further but marked for future improvements.

4.4 *Magnetic Field*

The effect of a magnetic field $\boldsymbol{B}$ on a particle with charge q and velocity $\boldsymbol{v}$ is described by the LORENTZ force,

$$F^i = q\varepsilon_{ijk}v^j B^k.$$

A discussion of the appearance of LANDAU *levels in graphene can for example be found in* LIBISCH, "Transition to Landau Levels in graphene quantum dots"*[19].*

Thus, a particle moving in the x-y plane under the influence of a magnetic field in z-direction always feels a force perpendicular to its motion. This results in circular orbits. Quantum mechanics forces the quantization of these cyclotron orbits, which are then called LANDAU levels.

The movement of electrons through a scattering structure is strongly influenced when the length scale of the cyclotron orbits approaches the system size. This is the case for strong magnetic fields and large structures, which is in general computationally difficult.

The mode basis decouples the computational time somewhat from the system size, as only a subset of modes is used. This makes the mode basis a promising candidate for computations involving magnetic fields. On the other hand, its conceptual starting point are the quantized modes in y direction which propagate in x direction. Under a strong field which forces the electrons into circular orbits the separation into x and y direction becomes meaningless. We thus cannot expect to be able to do computations with strong fields.

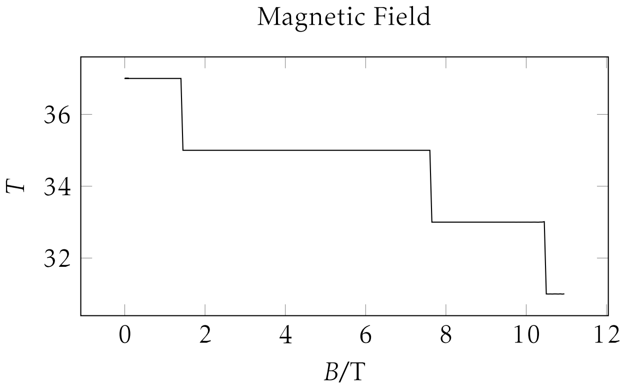

Figure 4.9: The appearance of Landau *Levels in a straight waveguide. The transmission (solid line) decreases with increasing magnetic field. The transverse system size is* 70 nm. *Parameters: 350 eigenvalues, 100 left and 100 right moving modes, 60 eigenfunctions of* $\mathcal{H}_0$*, 269 modes in total.*

Straight waveguide A magnetic field in z direction pushes an electron propagating in positive x direction through an electron waveguide a bit "to the side" into positive y direction. The electron wavefunction then no longer spreads through the whole structure, but occupies only the "upper" part in y-direction – just as if the electron waveguide would have been made narrower in y direction. In a narrower waveguide we have fewer propagating modes for a given energy. Hence, the transmission through an electron waveguide decreases with increasing magnetic field, see Fig. 4.9.

The mode basis captures this behaviour in a straight waveguide of width $W = 70\,\text{nm}$ described by 269 modes instead of 700 tight-binding orbitals for up to $B = 10\,\text{T}$. For larger fields, the calculation fails. This can be attributed to the recursive Green's function algorithm. Since the magnetic field is introduced via Peierl's substitution (see [18]) the single slices the geometry is build up from do not know about the magnetic field. The eigenfunctions of an infinite waveguide are strongly influenced by the field and hence are not a good basis set to describe a single slice without field.

Transport through edge states More interesting than a straight waveguide are structures like a cavity. Then we no longer have perfect transmission, but part of the current reflects back, $R \neq 0$. Interestingly, when the propagating states get pushed more and more towards the edge, they feel the effects of the geometry of the structure less and less. Once the right propagating states on the upper edge and the left-propagating states on the lower edge have vanishing overlap, there isn't even a chance for an electron to scatter back. This effect is connected to the quantum Hall effect.

For low magnetic fields, we observe the rise in transmission due to the beginning formation of transport through edge states, Fig. 4.10. At fields above 5 T, the calculation in the mode basis fails. It fails because it cannot describe changes in the transverse geometry. When the geometry gets wider or narrower the states propagate, under the influence of the magnetic field, along the edge in y direction.

A solution to this problem would be to calculate the region with

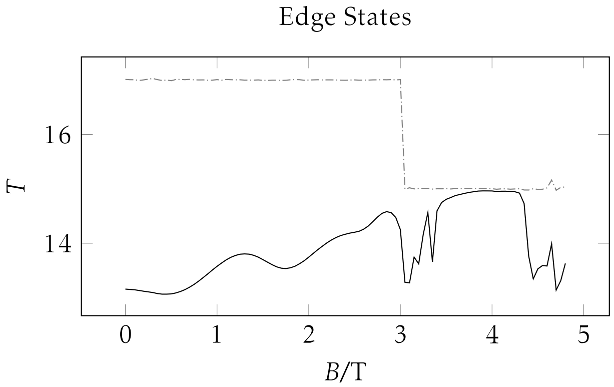

Figure 4.10: The number of modes, as given by transmission plus reflection (dashed line) decreases with increasing magnetic field. The transmission (solid line) generally increases due to the formation of edge states. A cavity of length $L = 80\,\mathrm{nm}$ *and width* $W = 90\,\mathrm{nm}$ *in a magnetic field. The transverse size of the leads is* $70\,\mathrm{nm}$. *Parameters (For personal use) 350 eigenvalues, 100 left and 100 right moving modes, 60 eigenfunctions of* $\mathcal{H}_0$, *269 modes (lead) and 271 modes (cavity) in total.*

changing transverse size in the position basis, and transform this block into the mode basis once the geometry doesn't undergo any more drastic changes. This point is marked for future work.

For moderately large fields however, we conclude that the mode basis is useful.

◆

Phonons

5

A description of phonons suitable for numerical calculations is obtained in Section 5.1. Phonon coupling in a straight waveguide is discussed in Section 5.2. To gain a better understanding of what controls phonon scattering events, we compare with the random walk model in Section 5.3. More complex geometries are considered in Section 5.4. We conclude this thesis by discussing more realistic phonon models in Section 5.5.

5.1 Electron - Phonon interaction

We use the Fröhlich Hamiltonian

$$\mathcal{H} = \sum_{\boldsymbol{k},s} \epsilon_{\boldsymbol{k},s} c^\dagger_{\boldsymbol{k},s} c_{\boldsymbol{k},s} + \sum_{\boldsymbol{q},v} \hbar\omega_{\boldsymbol{q},v} a^\dagger_{\boldsymbol{q},v} a_{\boldsymbol{q},v} + \sum_{\boldsymbol{k}\boldsymbol{k}'\boldsymbol{q}sv} \delta_{\boldsymbol{k}\boldsymbol{k}'\boldsymbol{q}sv} \left(a^\dagger_{-\boldsymbol{q},v} + a_{\boldsymbol{q},v} \right) c^\dagger_{\boldsymbol{k}',s} c_{\boldsymbol{k},s}$$

to describe the electron-phonon interaction. Here, $\epsilon_{\boldsymbol{k},s}$ is the (undisturbed) energy of an electron with wave vector $\boldsymbol{k}$ and spin s, $c^\dagger$ and c are the electron creation and annihilation operators, $\hbar\omega_{\boldsymbol{q},v}$ is the (undisturbed) energy of a phonon with wave vector $\boldsymbol{q}$ in branch v, $a^\dagger$ and a are the phonon creation and annihilation operators, and δ is the electron-phonon coupling element. Momentum conservation $\boldsymbol{k}' = \boldsymbol{k} + \boldsymbol{q}$ is enforced by the electron-phonon coupling element $\delta_{\boldsymbol{k}\boldsymbol{k}'qsv}$.

Phonon model for numerical calculations Next, we motivate certain simplifications. Let us choose a single, optical phonon branch, and assume vanishing dispersion and a constant density of states. Then the summation over v is fixed and also the $\boldsymbol{q}$ dependence vanishes. Further, let us assume that the electron-phonon coupling δ is constant and small. An electron with initial wave vector $\boldsymbol{k}$ has the chance to excite or absorb a phonon with energy $\hbar\omega$ at a certain point in the scattering structure. Their probability to scatter multiple times is damped in powers of δ.

We discuss the possible relaxations of these stringent assumptions in Section 5.5. All calculations in this thesis however focus on this heavily simplified picture. In a first step, we only want to understand what an electron does when it has the possibility to loose or gain energy, without putting too much information into the inelastic scattering process itself.

Let us cast this into a form which can be used in numerical calculations. We denote the undisturbed Hamiltonian by $\mathcal{H}_0$. The matrix δ now couples $\mathcal{H}_0$ to the Hamiltonian $\mathcal{H}_{\pm 1}$ which describes the same situation, except with an additional energy ±$\hbar\omega$ from one

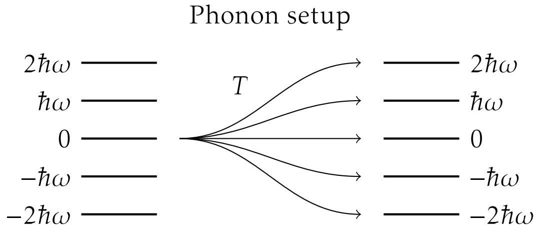

Figure 5.1: Reflection and Transmission coefficients are computed for an incoming electron at energy shift $\hbar\omega = 0\,\mathrm{eV}$. It can either reflect into one of the energy sheets on the left (not shown), or go into one of the sheets on the right. The transmission plus the reflection equals the number of open modes $T + R = N_{modes}$ in the sheet $\hbar\omega = 0\,\mathrm{eV}$.

phonon scattering event. In matrix form we have

$$\mathcal{H} = \begin{pmatrix} \ddots & \ddots & & & \\ \ddots & \mathcal{H}_{+\hbar\omega} & \delta & & \\ & \delta & \mathcal{H}_0 & \delta & \\ & & \delta & \mathcal{H}_{-\hbar\omega} & \ddots \\ & & & \ddots & \ddots \end{pmatrix}. \tag{5.1}$$

This of course is an infinite matrix. Assuming that the coupling δ is weak, we can introduce a cut off at some point, which renders the matrix finite dimensional. In this thesis we present transport calculations through a structure described by such a HAMILTONIAN with the help of a transformation into the mode basis.

A TAYLOR *expansion in powers of δ seems to be unstable, see Appendix A.*

This kind of "multilayer Hamiltonian" may be used to describe either (weakly coupled) multilayer systems, or certain interactions. For example, one can interpret it as "few layer graphene with a potential gradient".

Further, it appears when one uses FLOQUET -theory to describe the HAMILTONIAN with an additional time periodic electromagnetic field, see [9] . In this case, the additional energy $\hbar\omega$ comes from a photon absorption process.

"FLOQUET-BLOCH Theory and Topology in Periodically Driven Lattices" by GÓMEZ LEÓN and PLATERO [9].

5.1.1 *Model System*

In Fig. 5.1 we show the general setup of a calculation with coupled energy-sheets. In addition to the HAMILTONIAN of the scattering structure at energy E, we do the calculation at energies spaced multiples of a small shift $\pm\hbar\omega$ apart. These equations are coupled, so an electron coming in at $\hbar\omega = 0\,\mathrm{eV}$ can either reflect into one of the energy sheets on the left or go into one of the sheets on the right (see Fig. 5.1). As the coupling between the individual sheets is assumed to be small, the main contribution typically comes from the sheet at $\hbar\omega = 0\,\mathrm{eV}$.

The resulting transmission curve is plotted as a stacked plot of the transmission into the individual E-sheets, see for example Fig. 5.2. In the lowest curve, the electron has gained the energy $n\hbar\omega$ (in Fig. 5.1 $n = 2$), and on top is the curves where the electron has lost the energy $n\hbar\omega$. As it is a stacked plot, the upper curve is also the total

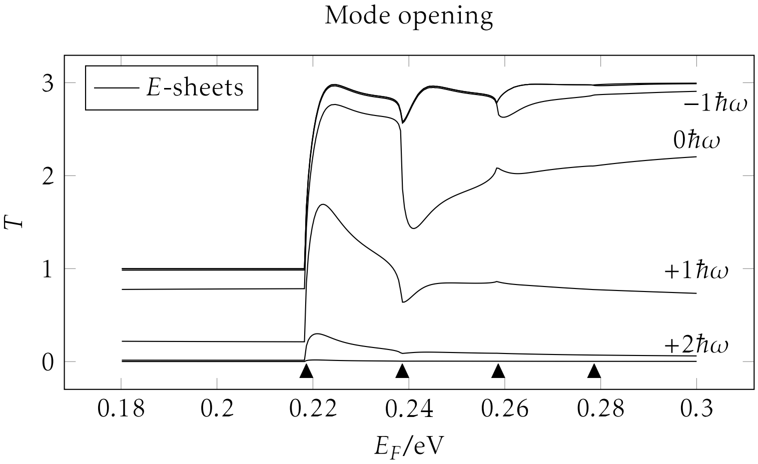

Figure 5.2: Transmission at the opening of a new mode in a combined calculation of 7 energy sheets separated by $\hbar\omega = 0.02\,\text{eV}$ *(black triangles). The individual transmission curves are shown as a stacked plot and labelled by* $-3\hbar\omega, \ldots 3\hbar\omega$*. The transverse system size is* $10\,\text{nm}$*, and phonon coupling is turned on for a length of* $20\,\text{nm}$*. Parameters: 50 eigenvalues, 14 left and 14 right moving modes, 13 eigenfunctions of* $\mathcal{H}_0$ *and the phonon coupling parameter is* $\delta = 0.01$.

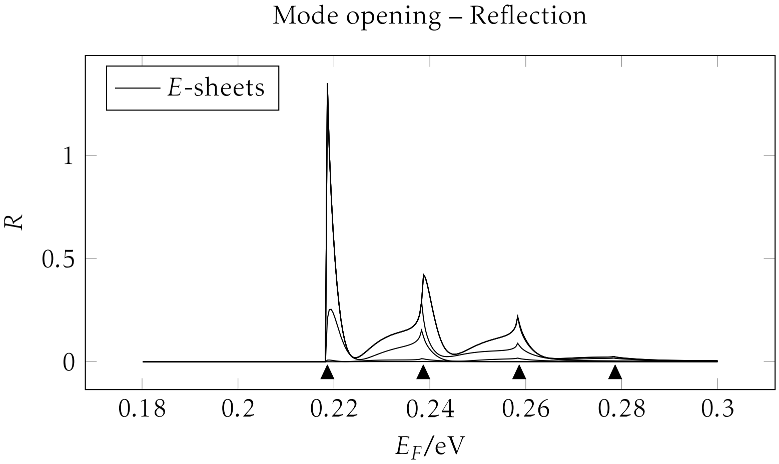

Figure 5.3: The Reflection coefficient corresponding to the calculation in Fig. 5.2. The opening of a new mode (black triangles) in a combined calculation of 7 energy sheets separated by $0.02\,\text{eV}$ *(black triangles). Shown is a stacked plot as discussed in Fig. 5.2. The system size is* $10\,\text{nm}$*, and phonon coupling is turned on for a length of* $20\,\text{nm}$*. Parameters: 50 eigenvalues, 14 left and 14 right moving modes, 13 eigenfunctions of* $\mathcal{H}_0$ *and the phonon coupling parameter is* $\delta = 0.01$.

transmission. Features in the individual transmission curves appear generally earlier in the lower curves, and later in the upper curves, and the total transmission is then smoothed out.

5.2 *Mode Opening*

We look at the effect of a mode opening in a waveguide. We combine 7 energy sheets separated by $\hbar\omega = 0.02\,\text{eV}$ in a calculation. The transmission of an incoming electron to the 7 sheets with the energy differences between $-3\hbar\omega, \ldots, 3\hbar\omega$ is computed, see Fig. 5.1.

The main contribution to the transmission far away from a mode opening comes from the sheet at $\hbar\omega = 0\,\text{eV}$ into itself, see for example the region around $E = 0.2\,\text{eV}$ in Fig. 5.2. There is also an important contribution into the sheets "above" and "below" in energy $\pm\hbar\omega$, and a small contribution into sheets 2 and 6. The coupling into sheet 1 and sheet 7 is (equally) small, and almost negligible.

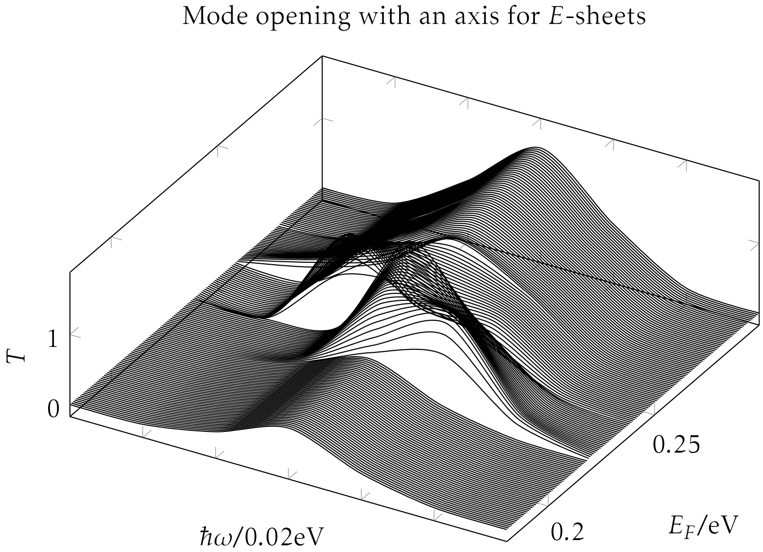

Figure 5.4: Transmission at the opening of a new mode in a combined calculation of 7 energy sheets separated by $\hbar\omega = 0.02\,\text{eV}$. *This is the same data as in Fig. 5.2, but an additional axis is introduced to separate the energy sheets. With increasing energy (labeled by E_F/eV), the mode opens. The transmission into the individual sheets (labeled by $\hbar\omega$/0.02eV) changes accordingly, see text. Smooth curves connect the energy sheets at equal energies.*

At $\approx E = 0.22\,\text{eV}$ a new mode opens up for the sheet at $\hbar\omega = 0\,\text{eV}$. At this point, the mode is already open in the sheets with addition energy $+1\hbar\omega, +2\hbar\omega, +3\hbar\omega$, and we can see transmission into all of these sheets.

We remark that we do not plot the transmission from the closed mode in sheet 4 just below $E = 0.22\,\text{eV}$ into the already open modes in the sheets $+1\hbar\omega, +2\hbar\omega, +3\hbar\omega$.

At $\approx E = 0.24\text{eV}$, the second mode opens for the sheet with $E = E_0 - 1\hbar\omega$. The energy at which this happens is exactly $\hbar\omega = 0.02\,\text{eV}$ above the energy of the mode opening of sheet 4. We observe a slight drop in transmission leading up to this point. At little higher energy, the transmission into sheet $-1\hbar\omega$ becomes the main contribution for a short energy range.

Pierrat *et al. investigate the dwell time of a wave through complex structures, but also through a clean waveguide in* "Invariance property of wave scattering through disordered media"*[23].*

These features can be attributed to the large dwell time of the new mode. The new mode has a high transverse momentum component, but only a small component into the propagating direction; it travels only slowly through the waveguide. This increases the chance of phonon scattering, and effectively increases the phonon coupling parameter. This shifts a significant part of the transmission into the newly open mode. Right before this mode opens we have a very similar situation, except that the mode doesn't propagate, but it decays into the waveguide. An electron has now the chance to scatter into this decaying mode. This mode in turn has a relatively strong coupling to left-moving modes, so the electron may scatter back, which leads to a small increase in the reflection. Inspection of the reflection curve Fig. 5.3 supports this argument. The main contribution to the reflection is from the energy sheet where the mode opening occurs.

At further multiples of $\hbar\omega = 0.02\,\text{eV}$ the mode opens in the other sheets and we can again observe a slight drop in the total transmission, followed by an increase in the transmission into this sheet, before everything stabilizes.

For visualization purposes, we introduce an additional axis for the individual sheets separated by $\hbar\omega$ in Fig. 5.4. The distinct mode openings can be well identified. Further, the transmission into the different energy sheets from the incoming sheet at $\hbar\omega = 0$ resemble a GAUSSIAN. This point is further elaborated in Section 5.3.

5.2.1 *Phonon coupling in a perfect waveguide*

Once we understand what happens at a mode opening, we can interpret the transmission through a perfect waveguide with phonons over a larger energy range, Fig. 5.5. At the mode openings, we can recognize the behaviour discussed in the last section. Far away from the mode openings, the transmission into the individual sheets stabilizes and the largest contribution stems from the sheet $\hbar\omega = 0$

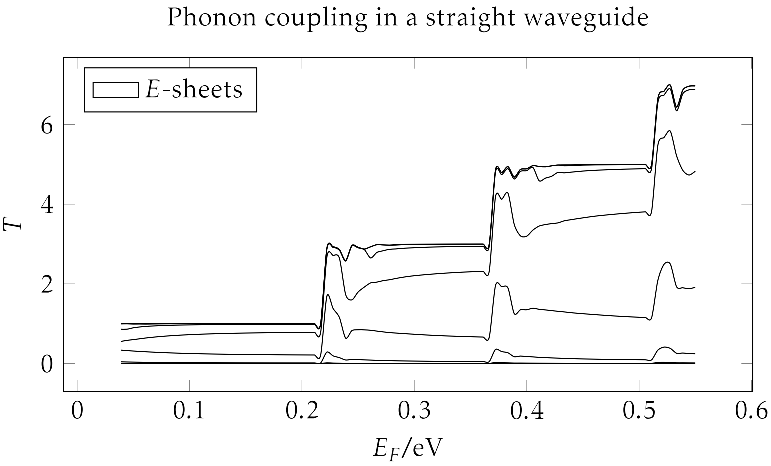

Figure 5.5: The transmission through a perfect waveguide as a combined calculation of 9 energy sheets separated by 0.02 eV. *Shown is a stacked plot as discussed in Fig. 5.2. The system size is* 10 nm, *and phonon coupling is turned on for a length of* 20 nm. *Parameters: 50 eigenvalues, 14 left and 14 right moving modes, 13 eigenfunctions of $\mathcal{H}_0$ and the phonon coupling parameter is $\delta = 0.01$.*

5.3 *Random Walk model*

Let us investigate the approximately GAUSSIAN spread into energy levels more closely. We fit a GAUSSIAN to the transmission into the different energy sheets and obtain good agreement, see Fig. 5.6. How can we understand this?

The random walk is a simple model for the transmission into the different energy sheets. Electron-phonon scattering may occur at each point in the geometry. The probability of such an event is by FERMI's golden rule the matrix element - the phonon coupling strength δ times the overlap between the initial and final wavefunctions squared, $p = |\delta|^2 \left|\langle\psi_i|\psi_f\rangle\right|^2$. The overlap depends on the transverse $\boldsymbol{k}$ vectors of the two wavefunction, $k_y(E)$ and $k_y(E \pm \hbar\omega)$. Let us assume that the overlap does not change considerably at the order of $\hbar\omega$ in E, $\langle\psi(E-\hbar\omega)\big|\psi(E)\rangle \approx \langle\psi(E)\big|\psi(E+\hbar\omega)\rangle$. Finally we assume a constant density of states at the order of $\hbar\omega$ in E. In this approximation, the probabilities to absorb or excite a phonon at each step is equal to p, and the probability to undergo no scattering is $1 - 2p$.

The probability for a path with N steps through the structure, where a phonon is excited n_+ and absorbed n_- times, and n_0 times no

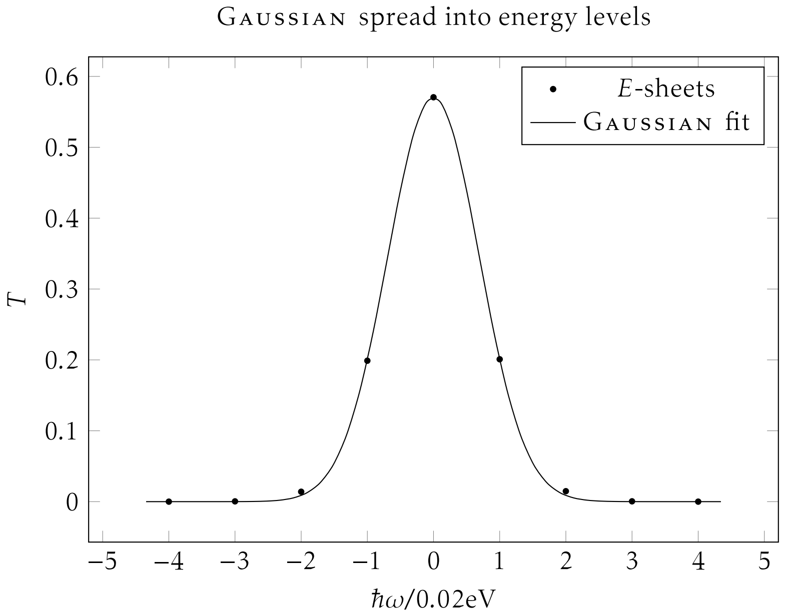

Figure 5.6: The approximately GAUSSIAN *spread of an incoming electron with* $0\hbar\omega$ *into different energy levels separated by* $\pm\hbar\omega$. *The random walk model (see Section 5.3) provides a simple picture for this behaviour. The data is the energy point at* $E = 0.216\,667\,\text{eV}$ *from the plot in Fig. 5.5*

phonon scattering occurs, is given by the multinomial distribution

$$f(n_+, n_-, n_0; N) = \frac{N!}{n_+! n_-! n_0!} p^{n_+ + n_-} (1-2p)^{n_0}.$$

In this step, we are neglecting possible interference terms.

The probability to end up with m excited phonons after N steps can be obtained by summing over all paths with $n_+ - n_- = m$,

$$f(m) = \sum_i^{i_{\max}} f(m+i, i, N-m-2i; N),$$

where $i_{\max} = (N-m)/2$, which is the situation where a phonon is excited or absorbed in each step and $n_0 = 0$. After rearranging terms, the sum can be written as the GAUSSIAN hypergeometric function ${}_2F_1$,

$$f(m) = \frac{N!}{(N-m)!m!} p^m (1-2p)^{N-m} {}_2F_1\Big((m-N)/2, (m-N+1)/2, m+1, 4p^2/(1-2p)^2\Big). \tag{5.2}$$

We have to do a fit on the full calculation to obtain the proportionality between p and δ^2.

The correctness of the model can be checked by fitting the probability p of the random walk model to calculations with the GREEN's function method for various values of δ. According to the model, the probability should, following FERMI's golden rule, be proportional to the square of δ, $p \propto \delta$. To this end, we calculate the transmission through a waveguide of width $W = 10\,\text{nm}$ at 9 energies around $E = 0.2\,\text{eV}$ with coupling turned on for $20\,\text{nm}$, and coupling strengths between $\delta = 0.001$ and $\delta = 0.01$. For larger coupling strength, a larger contribution to the total transmission comes from energy-sheets with $\hbar\omega \neq 0$, see Fig. 5.7. The spread into the different energy values obtained with the random walk model, Eq. (5.2), is in good agreement with the full calculation Fig. 5.8. Deviations from the

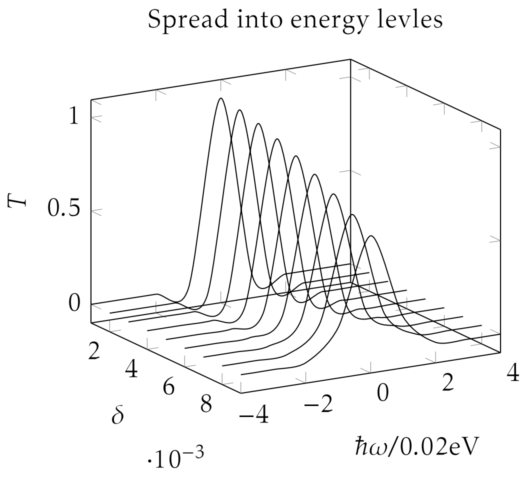

Figure 5.7: Transmission into the individual E-sheets for a waveguide of $W = 10\,\mathrm{nm}$ *at 9 energies around* $E = 0.2\,\mathrm{eV}$ *with coupling turned on for* $20\,\mathrm{nm}$, *and coupling between* $\delta = 0.001$ *and* $\delta = 0.01$. *A smooth curve connects the data points at equal energies.*

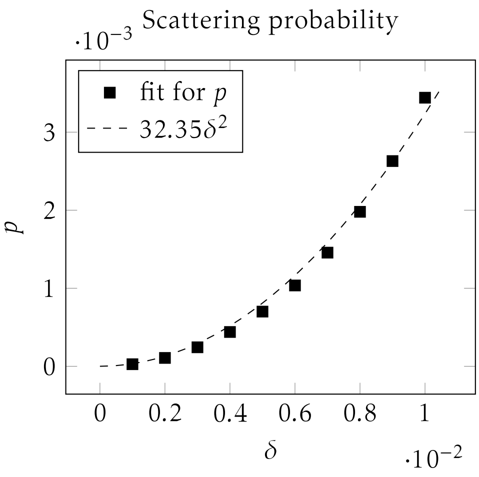

Figure 5.8: Fit of the scattering probability p (black points) as determined to the random walk model Eq. (5.2) to the full calculation. The probability for a scattering event in the random walk model is proportional to the square of the phonon coupling δ in the mode basis calculation, $p \propto \delta^2$. *(dashed line)*

model (see Fig. 5.8) do not come as a surprise, as the random walk model does not take varying overlap $\langle\psi(E)|\psi(E')\rangle$, the finite number of energy sheets, interference effects as well as paths which traverse the structure in other than N steps (via multiple reflections) into account.

The good agreement with the calculation in the mode basis suggests that the random walk model is an interesting candidate for Monte-Carlo simulations that include phonon scattering “by hand”.

5.4 Building Blocks

5.4.1 Constriction, with phonons

We go to more complex structures and calculate the transmission through a constriction with phonons, Fig. 5.9. Eigenstates of the constriction couple strongly to the wide leads and are very broad. By close inspection of the data we observe that the transmission into the sheets with additional energy $+3\hbar\omega, \ldots + \hbar\omega$ rises before the transmission in the sheet $\hbar\omega = 0\,\mathrm{eV}$ rises. Therefore peaks or dips appear sooner (later) in the sheets with $+n\hbar\omega$ ($+n\hbar\omega$). In contrast to the exact calculation (Fig. 4.3) features in the total transmission get smeared out. However, these smooth peaks do not appear $\hbar\omega$ spaced apart in the individual transmission curves, but much closer in energy. This is because the phonon scattering can occur at any point in the structure which leads to a continuous increase in transmission.

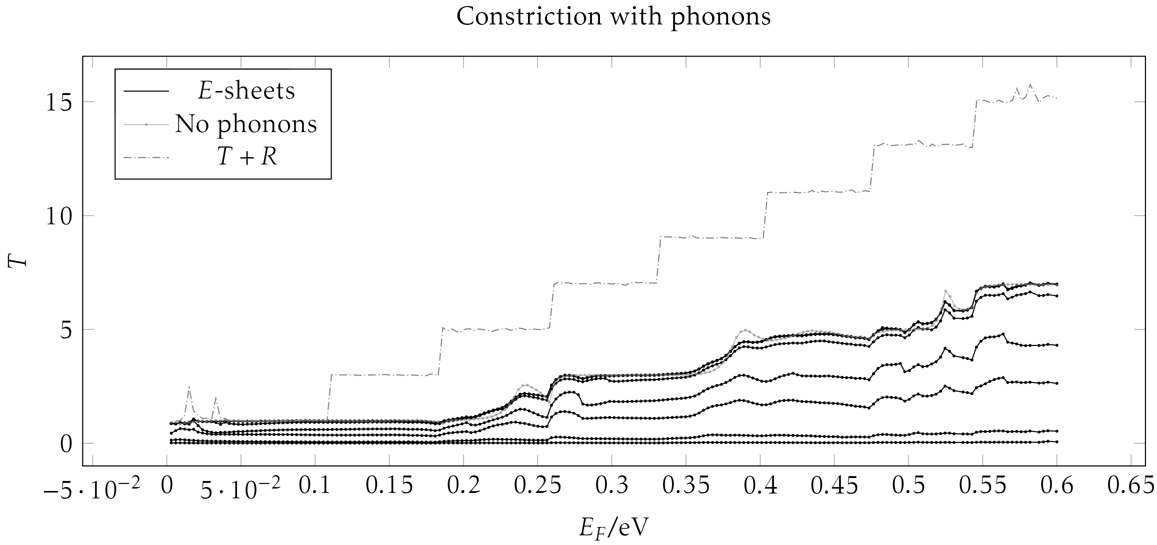

Figure 5.9: The plot shows the tunneling though a constriction in a combined calculation of 7 energy sheets separated by 0.02 eV. *Shown is a stacked plot as discussed in Fig. 5.2. The exact calculation is shown in Fig. 4.3. The leads have a width of* 20 nm, *and the constriction has a width of* 10 nm. *Phonon coupling is turned on* 10 nm *before the constriction and turned off* 10 nm *after the constriction. Parameters: 50 eigenvalues, 14 left and 14 right moving modes, 10 eigenfunctions of* $\mathcal{H}_0$ *for the constriction, 80 eigenvalues, 20 left and 20 right moving modes, 12 eigenfunctions of* $\mathcal{H}_0$ *for the leads, and the phonon coupling parameter is* $\delta = 0.01$.

5.4.2 *Cavity, with phonons, sharp peaks*

The transmission curve of a large cavity ($W = 50$nm and length $L = 40$nm) with small leads ($W = 10$nm) at low energies is comparatively easy to interpret, see Fig. 5.10. Eigenstate of the cavity, which couple weakly to the leads show up as sharp resonances in the transmission curve. We observe Broad peaks, sharp Breit-Wigner resonances and window resonances.

For an introduction to Fano *resonances, see Section 2.2*

Let us discuss the effect of phonon scattering on the transmission curve. Broad features get smeared out, as already discussed for the constriction. In this calculation, we observe a large peak between $E = 0.172$eV and $E = 0.189$eV. The transmission into the sheet with energy shift $\hbar\omega = 0.005$eV begins to rise exactly 0.005eV earlier, and the transmission into sheet with energy $\hbar\omega = -0.005$eV rises 0.005eV later. (The arrows in Fig. 5.10 point to the discussed features). This results in a slightly decreased transmission compared to the calculation without phonons.

A dip in the total transmission at $E = 0.172$eV *superposes the rise into the lower energy sheet. It is therefore a bit harder to discern.*

Tunneling via weakly coupled eigenstates of the cavity results in sharp Breit-Wigner resonances. We observe a distinct sharp peak at $E = 0.104$eV, and due to resonance in the corresponding phonon-sheet, a smaller peak at $E = 0.109$eV. We also observe a rise in transmission into the sheet with $\delta E = \hbar\omega$ at $E = 0.104$eV. When transport via such an eigenstate takes place, its longevity enhances the chance of phonon scattering. This leads to an increase in the transmission into the neighbouring energy sheets, while the total transmission is unaffected. At certain points, however

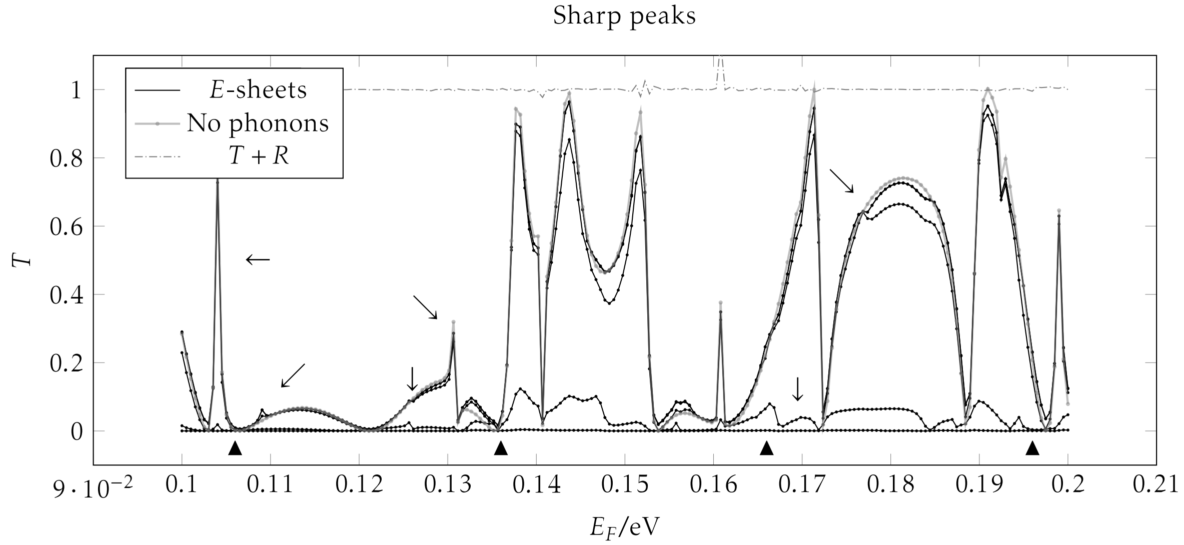

Figure 5.10: Transmission through a cavity of width $W = 50\,\mathrm{nm}$ *and length* $L = 40\,\mathrm{nm}$, *the leads are* $W = 10\,\mathrm{nm}$ *wide. Shown is a stacked plot as discussed in Fig. 5.2. Phonon coupling between the 5 energy sheets separated by* $\hbar\omega = 0.005\,\mathrm{eV}$ *is turned on* $20\,\mathrm{nm}$ *before the cavity and turned off* $40\,\mathrm{nm}$ *after it. Black triangles indicate the positions of mode openings in the* $W = 50\,\mathrm{nm}$ *wide region. Parameters: The phonon coupling is* $\delta = -0.001$. *We use 50 eigenvalues for the leads, 14 right- and left moving basis vectors, and 10 eigenvectors for* $\mathcal{H}_0$. *For the cavity, 160 eigenvalues, 50 right- and left moving basis vectors, and 20 eigenvectors for* $\mathcal{H}_0$.

(see $E = 0.104\,\mathrm{eV}$, or $E = 0.1605\,\mathrm{eV}$ in Fig. 5.10), we observe only a contribution of the sheet with the additional energy $\hbar\omega$. A possible explanation is that though coupling to the state $-\hbar\omega$ lower in energy exists, it is not a propagating state and doesn't contribute to the transmission.

Window resonances result from destructive interference with eigenstates of the cavity. Phonon coupling does not change the form or depth of these dips. Due to the destructive interference, the incoming electron never really enters the cavity and never has a chance to scatter on a phonon. Further, the window resonance does not appear at the characteristic energy shifts at multiples of $\hbar\omega = 0.005\,\mathrm{eV}$. This is because the electron-phonon scattering may occur at any position in the structure, thus the electron appears at any position in the sheets shifted in energy. This lifts the destructive interference.

In this discussion, we are talking about the scattering matrix of the cavity alone. Whenever we include large parts of the leads, inelastic scattering may already occur there. In that case, the electron has a different energy when entering the structure. Then, dips appear multiple times.

Cavity, with phonons

We compute the transmission through a cavity of width $W = 20\,\mathrm{nm}$, $L = 40\,\mathrm{nm}$, with leads of width $W = 10\,\mathrm{nm}$, (the same as in Fig. 4.4) with additional phonon coupling, see Fig. 5.11. The transmission curve shows many resonances of various shapes. At the individual resonances, one can observe the behaviour discussed in the last paragraphs. Peaks appear at the characteristic energy shifts at multiples of $\hbar\omega = 0.01\,\mathrm{eV}$. Thus, peaks larger than $\hbar\omega$ get smeared out, and peaks with a width smaller than $\hbar\omega$ appear multiple times.

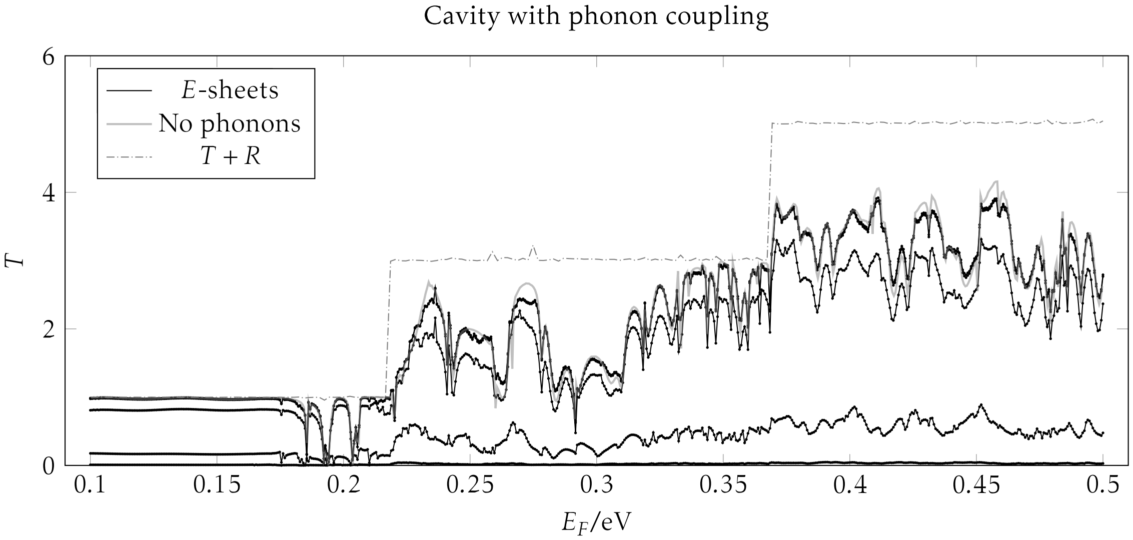

Figure 5.11: Transmission through a graphene scattering structure with following dimensions: Leads: $W = 10\,\mathrm{nm}$*, structure:* $W = 20\,\mathrm{nm}$, $L = 40\,\mathrm{nm}$*. The computation combines 5 energy sheets separated by* $\hbar\omega = 0.01\,\mathrm{eV}$*. Parameters in the calculation: 50 eigenvalues, 14 left and 14 right moving modes, 10 eigenfunctions of* $\mathcal{H}_0$ *for the* 10 nm*, and 90 eigenvalues, 22 left and 22 right moving modes, 16 eigenfunctions of* $\mathcal{H}_0$ *for the* 20 nm*. Phonon Coupling is turned on* 10 nm *before the cavity and turned off* 10 nm *after the cavity. The coupling strength is* $\delta = -0.003$.

Dips due to reflection are not changed by phonon coupling.

5.4.3 Barrier

A short barrier is considered in Fig. 5.13. The oscillations in the transmission curve for a wide barrier (Fig. 5.12) and the monotonic increase for a short barrier (Fig. 5.13) are well-known, see e.g. "Solid State Physics" *by* Grosso *and* Parravicini *[12].*

One of the most striking effects of inelastic scattering can be observed when considering a potential barrier with potential V. We choose a rather wide barrier, see Fig. 5.12, to suppress tunneling completely. Consequently the transmission in the calculation without inelastic scattering begins to rise when the incoming particle has enough energy $E > V$ to pass over the barrier.

In contrast we already observe non-vanishing transmission in the otherwise forbidden region several $\hbar\omega$ below V. This happens when the incoming particle gains additional energy by means of inelastic scattering and can therefore traverse the barrier.

At close inspection one can observe that the peaks appear $\hbar\omega$ spaced apart, see arrows in Fig. 5.12. Particularly, each of the multiple peaks can be traced down to its proper energy sheet.

Due to the stacked plot, it may look as if some peaks appear in multiple energy sheets, but one really has to consider the difference between adjacent sheets.

Short barrier, Tunneling.

Tunneling is important in very short barriers, see Fig. 5.13. We observe that (in our model) inelastic scattering does not change the transmission curve at all. This is due to the almost perfectly linear rise in transmission through the short barrier (see also [12]) and that in our model gaining and loosing energy are equally probable. Hence, everything which is lost in transmission by scattering into states with

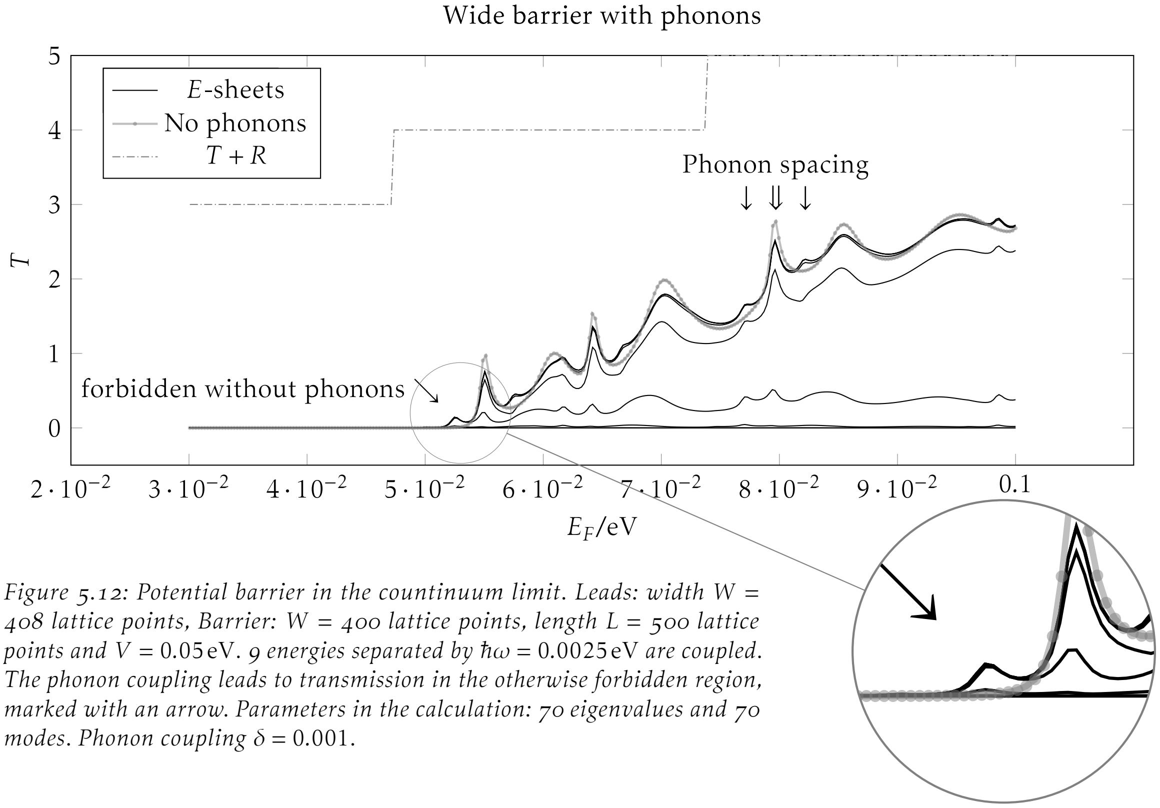

Figure 5.12: Potential barrier in the countinuum limit. Leads: width $W =$ *408 lattice points, Barrier:* $W = 400$ *lattice points, length* $L = 500$ *lattice points and* $V = 0.05\,\mathrm{eV}$. *9 energies separated by* $\hbar\omega = 0.0025\,\mathrm{eV}$ *are coupled. The phonon coupling leads to transmission in the otherwise forbidden region, marked with an arrow. Parameters in the calculation: 70 eigenvalues and 70 modes. Phonon coupling* $\delta = 0.001$.

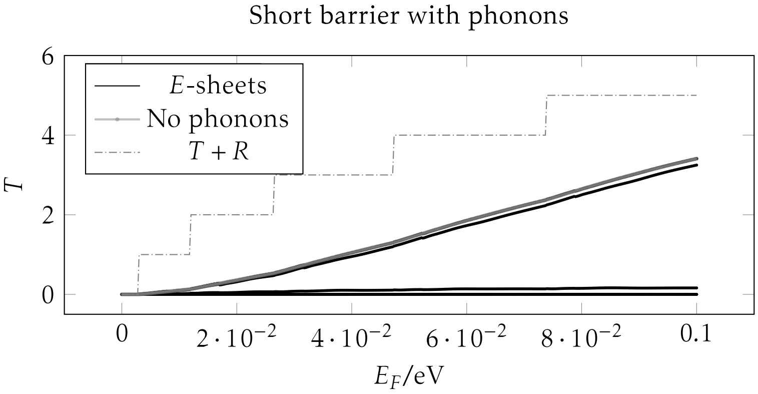

Figure 5.13: Transmission through a potential barrier in the continuum limit. The transmission with phonon coupling (black line) is identical to the transmission curve without phonons (gray line, overlaps one black line) Leads: width $W = 408$ *lattice points, Barrier:* $W = 400$ *lattice points, length* $L = 50$ *lattice points and* $V = 0.05\,\mathrm{eV}$. *9 energies separated by* $\hbar\omega = 0.0025\,\mathrm{eV}$ *are coupled. Parameters in the calculation: 70 eigenvalues and 70 modes. Phonon coupling* $\delta = 0.001$.

Double Barrier with phonons. Energy $\hbar\omega = 0.001\,\mathrm{eV}$ and coupling $\delta = 0.0005$.

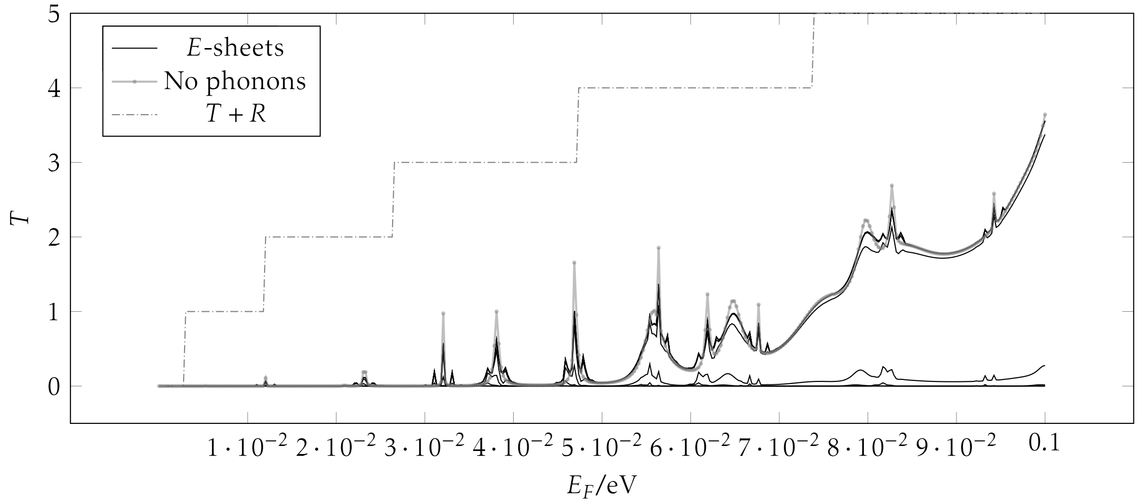

Double Barrier with phonons. Energy $\hbar\omega = 0.001\,\mathrm{eV}$ and coupling $\delta = 0.001$.

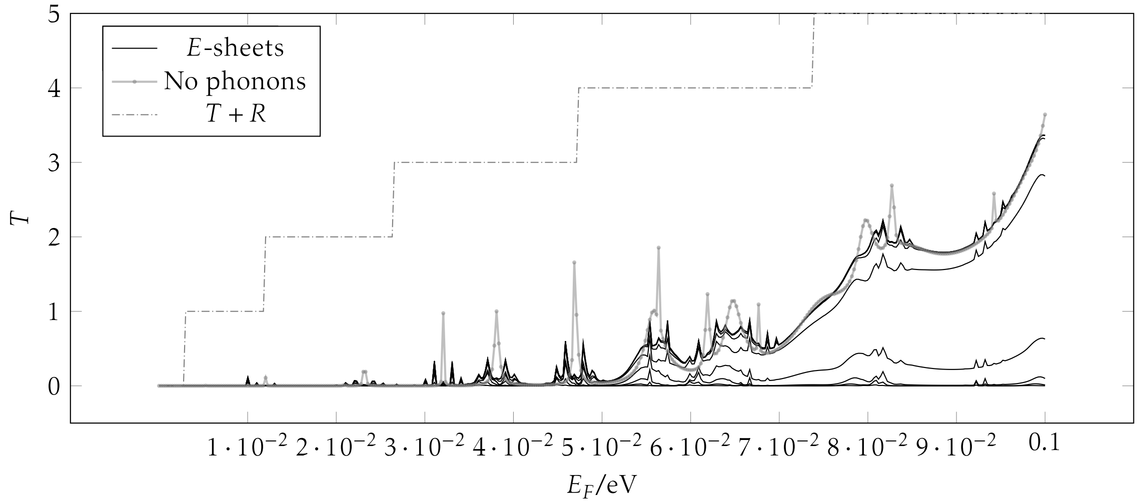

Figure 5.14: Potential barrier in the countinuum limit. Resonant tunneling can be observed at low energies $E < V$ (gray curve). Phonon coupling leads to a series of peaks around the resonat energy (black curves). Leads: width $W = 408$ lattice points, Barrier $W = 400$ lattice points, length $L = 100$ lattice points and $E = 0.05\,\mathrm{eV}$, then 400 lattice points and again a barrier of length $L = 100$ lattice points and $V = 0.05\,\mathrm{eV}$. 9 energies separated by $\hbar\omega = 0.001\,\mathrm{eV}$ are coupled. Parameters in the calculation: 70 eigenvalues and 70 modes. Phonon coupling $\delta = 0.0005$ and 0.001.

lower energy is balanced by the enhanced transmission of states with higher energy.

We do though observe very small dips due to mode openings in the sheet with additional energy $\hbar\omega$. This was already discussed in Section 5.2.

Double barrier, Resonant tunneling.

We conclude this section with resonant tunneling through a double barrier, see Fig. 5.14. The barrier height is $V = 0.05\,\text{eV}$. For lower energies $E < V$ the transmission is generally zero except at certain resonant energies. Phonon coupling leads to peaks in the transmission when the energy E equals a resonant energy, and also when the resonance can be reached by excitation or absorption of a phonon, $E \pm \hbar\omega$.

We further observe a curious phenomenon at strong phonon coupling and small phonon spacing. With increasing phonon coupling, the peak at the original resonant energy vanishes (see coupling $\delta = 0.001$ in Fig. 5.14). The peaks corresponding to one phonon scattering event are enhanced. It is most likely related to the long dwell time of the resonant state, which increases the chance of a phonon scattering event. No clear explanation can be given at the moment, but it probably is an interference phenomenon. At even higher phonon coupling (see $\delta = 0.0015$ in Fig. 5.14) the most prominent peaks correspond to two scattering events. At close inspection, the width of the resonance is larger than the phonon spacing $\hbar\omega$, and therefore the dwell time of the states corresponding to phonon scattering is still slightly enhanced.

A check for this argument provides a further calculation (not shown) with larger spacing $\hbar\omega = 0.002\,\text{eV}$ and correspondingly larger coupling $\delta = 0.002$. Now the state with additional $\pm\hbar\omega$ is away from resonance and constitutes the largest contribution.

This coupling is effectively of the same strength as $\delta = 0.0015$ *for* $\hbar\omega = 0.001\,\text{eV}$ *in the sense that now the spread into the individual energy sheets away from resonances is approximately equal.*

Energy renormalization

Let us consider a two-level system with weak coupling and energies spaced $\hbar\omega$ apart or, in our phonon-picture, the situation where we can excite exactly one phonon. The asymmetry in this setup lets us observe energy renormalization, see Fig. 5.15. Through the mutual interaction, the states at resonant energies E_r and $E_r - \hbar\omega$ repel each other, as predicted by perturbation theory. They are further apart when the interaction is stronger.

5.5 *Towards a more realistic phonon model*

Up to now, we have implemented phonon coupling via a single constant denoted by δ, see Eq. (5.1). It is possible to include more physical information by making this parameter dependent on the electron energy, the phonon energy, or on the position in the crystal.

Density of States The probability p for electron-phonon scattering is proportional to the phonon-density of states $D(\hbar\omega)$. One can include this information into an effective coupling constant, $\delta = \delta(\hbar\omega)$. We have shown in the section on the random walk model, Section 5.3, that the scattering probability is, by Fermi's golden rule, proportional to the square of the coupling parameter $p \propto \delta^2$. Thus, an effective

Double Barrier with phonons. Energy $\hbar\omega = 0.001\,\mathrm{eV}$ and coupling $\delta = 0.001$.

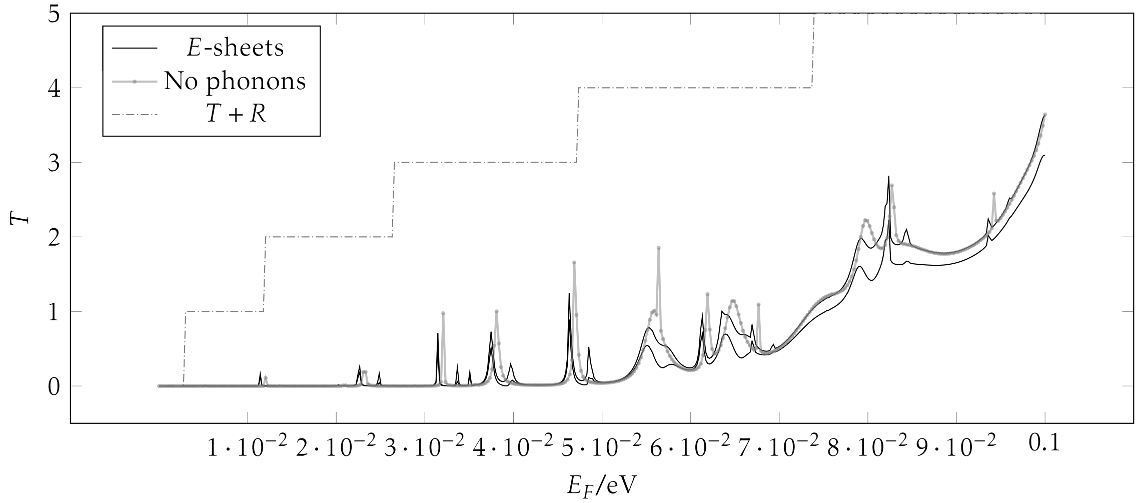

Double Barrier with phonons. Energy $\hbar\omega = 0.001\,\mathrm{eV}$ and coupling $\delta = 0.002$.

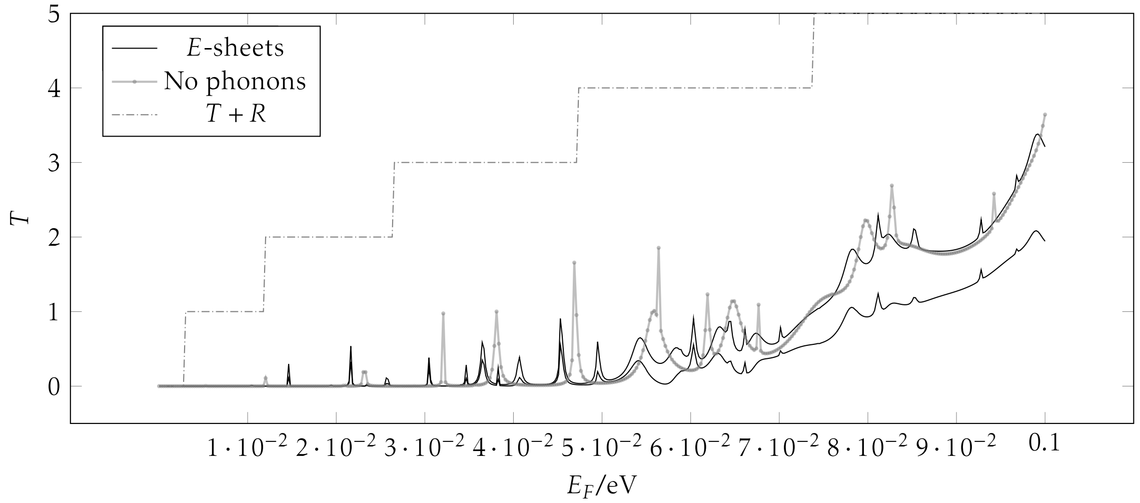

Figure 5.15: Potential barrier in the countinuum limit. The energy renormalization due to the phonon interaction shifts the levels (black curve) away from the resonant energies without phonons (gray curve). Leads: width $W = 408$ lattice points, Barrier $W = 400$ lattice points, length $L = 100$ lattice points and $E = 0.05\,\mathrm{eV}$, then 400 lattice points and again a barrier of length $L = 100$ lattice points and $E = 0.05\,\mathrm{eV}$. 2 energies separated by $\hbar\omega = 0.001\,\mathrm{eV}$ are coupled. Parameters in the calculation: 70 eigenvalues and 70 modes. Phonon coupling $\delta = 0.001$ and 0.001.

coupling parameter which describes these phase space effects would be $\tilde{\delta} = \delta\sqrt{D(\hbar\omega)}$.

Interference and Decoherence The calculation, as described by the Hamiltonain in Eq. (5.1) is fully coherent. Decoherence by phonons is introduced by summing over the total transmissions into the individual energy sheets, $T_{\text{total}} = \ldots + T_{-1\hbar\omega} + T_{0\hbar\omega} + T_{+1\hbar\omega} + \ldots$.

Realistically, every phonon scattering event randomizes the phase $\Delta\phi$ of the scattering electron, $\tilde{\delta} = \delta \exp \mathrm{i}\Delta\phi$. This can be implemented by averaging over various realizations of a system, where a (small) random phase $\Delta\phi$ is assigned to the coupling constant δ at each point. An approximation to this is to neglect the y-dependence of the random phase. Then the matrix $\mathbb{1}\delta \exp \mathrm{i}\Delta\phi(x)$ is still proportional to unity and calculations are much more efficient since one does not have to do the costly matrix inversions at every slice.

Conclusion & Outlook

6

We have shown (Chapter 3) that the mode basis is in most cases a fast and accurate approximation of the exact calculation. Especially for a non-separable HAMILTONIAN the stability of the mode basis depends crucially on which modes are included (Section 3.3). Future work will especially focus on the problems with resonant eigenstates and strong magnetic fields. Solving individual "difficult" parts of the geometry featuring e.g. point defects in the position basis can improve accuracy without strongly affecting execution speed.

The current proof of concept implementation already reveals many non-trivial effects of electron-phonon interaction. Sharp peaks in the original transmission curve appear multiple times, broad peaks become smeared out. By contrast, dips remain unaffected (Section 5.4). A very important short term goal is to parallelize and modularize the mode basis code. This is of interest for the expensive coupled calculations which describe inelastic scattering. From the number of required modes in our calculations and the performance of the fully modular and parallel code in the position basis we extrapolate that we will be able to couple up to 20 phonon excitations for graphene and up to 50 for the continuum limit HAMILTONIAN . More realistic models than the current single optical phonon branch can then be implemented.

⁂

Things that do not work

A

In our quest to describe transport at multiple energies at once, we first tried to exploit the small coupling between different energies and use a Taylor expansion in the coupling parameter. We elaborate on this idea in the following section. However, the first order Taylor expansion turns out to be numerically unstable, assumedly because the small errors introduced in each step lead to over-coupling into exponentially increasing modes. A higher order Taylor expansion already couples all matrix elements and we gain no computational advantage compared to the exact calculation.

This section is included for completeness, and probably mostly of relevance for someone who tries to implement similar ideas.

A.1 Expansion in Phonon Coupling

We computed the exact equations of the recursive Green's function method in Section 2.5.1. The first order Taylor expansion in the coupling parameter δ of Eq. (5.1) can be obtained as follows.

First, we calculate the diagonal blocks without phonon interactions

$$\tilde{\mathcal{G}}_{33,\mathrm{Diag}} \approx \left(E - \mathcal{H} - \mathcal{H}_I^\dagger \mathcal{G}_{22,\mathrm{Diag}} \mathcal{H}_I\right)^{-1}$$

We then invert the Hamiltonian of the new slice in first order in δ. This can be done without inverting the full matrix. We thereby obtain a tri-diagonal matrix $\tilde{\mathcal{G}}_{33,\mathrm{TriDiag}}$. Phonon coupling is then incorporated by expanding Dyson's equation in first order,

$$\begin{aligned}\tilde{\mathcal{G}}_{33} \approx \tilde{\mathcal{G}}_{33,\mathrm{Diag}} &+ \mathcal{G}_{33,\mathrm{TriDiag}} \mathcal{H}_I^\dagger \mathcal{G}_{22} \mathcal{H}_I \mathcal{G}_{33,\mathrm{TriDiag}} \\ &- \mathcal{G}_{33,\mathrm{Diag}} \mathcal{H}_I^\dagger \mathcal{G}_{22,\mathrm{Diag}} \mathcal{H}_I \mathcal{G}_{33,\mathrm{Diag}}.\end{aligned}$$

In this equation, the diagonal term $\mathcal{G}_{33,\mathrm{Diag}} \mathcal{H}_I^\dagger \mathcal{G}_{22,\mathrm{Diag}} \mathcal{H}_I \mathcal{G}_{33,\mathrm{Diag}}$ has to be subtracted form the full $\mathcal{G}_{33,\mathrm{TriDiag}} \mathcal{H}_I^\dagger \mathcal{G}_{22} \mathcal{H}_I \mathcal{G}_{33,\mathrm{TriDiag}}$, since the diagonal terms are already contained in the exact $\tilde{\mathcal{G}}_{33,\mathrm{Diag}}$. The Green's functions $\tilde{\mathcal{G}}_{31}$ and $\tilde{\mathcal{G}}_{13}$ can now easily be computed. Again, we keep only the largest parts by multiplying only with the (block) tri-diagonal part of $\tilde{\mathcal{G}}_{33}$,

$$\begin{aligned}\tilde{\mathcal{G}}_{31} &\approx \tilde{\mathcal{G}}_{33,\mathrm{TriDiag}} \mathcal{H}_I^\dagger \mathcal{G}_{21} \\ \tilde{\mathcal{G}}_{13} &\approx \mathcal{G}_{12} \mathcal{H}_I \tilde{\mathcal{G}}_{33,\mathrm{TriDiag}}.\end{aligned}$$

The Green's function $\mathcal{G}_{11}$ cannot be obtained from a Taylor expansion in first order. The suggested solution is to do the computation from both sides, since $\mathcal{G}_{33}$ can be obtained easily.

This procedure is unfortunately unstable.

A.2 Alternative: Phonon Coupling over H_I

As an alternative, we can introduce the coupling via the interaction Hamiltonian H_I. This has the advantage, that in the limit of the

GREEN's function $\mathcal{G}_{22}$ of the existing block being equal the one with one slice attached $\mathcal{G}_{33}$ (thus, in the limit of a semi-infinite lead) almost all paths are included: The paths not included are those going from the new slice to the existing block, back to the new slice, back to the exisiting block, and back to the new slice and thereby undergoing two or more phonon scattering events (see equations).

Phonon Coupling over H_I decouples the equations for $\tilde{\mathcal{G}}_{33}$. We write down all the paths which connect back to the new slice:

$$\begin{aligned}\tilde{\mathcal{G}}^{ii}_{33} = \mathcal{G}^{ii}_{33} &+ \mathcal{G}^{ii}_{33}\mathcal{H}_I^{\dagger}\mathcal{G}^{ii}_{22}\mathcal{H}_I\mathcal{G}^{ii}_{33}\\ &+ \mathcal{G}^{ii}_{33}\delta^{\dagger}\left(\mathcal{G}^{(i+1)i}_{22} + \mathcal{G}^{(i-1)i}_{22}\right)\mathcal{H}_I\mathcal{G}^{ii}_{33}\\ &+ \mathcal{G}^{ii}_{33}\mathcal{H}_I^{\dagger}\left(\mathcal{G}^{i(i+1)}_{22} + \mathcal{G}^{i(i-1)}_{22}\right)\delta\mathcal{G}^{ii}_{33}\\ &+ \mathcal{G}^{ii}_{33}\delta^{\dagger}\left(\mathcal{G}^{(i+1)(i+1)}_{22} + \mathcal{G}^{(i-1)(i-1)}_{22}\right)\delta\mathcal{G}^{ii}_{33} + \dots.\end{aligned}$$

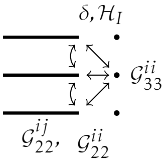

Figure A.1: Phonon coupling via the interaction Hamiltonian. Different layers correspond to different phonon numbers. The interaction between the layers is described by the interaction matrix δ*. For a general block, there will be non-zero off-diagonal elements* $\mathcal{G}^{ij}_{22}$

The upper indices in this expression specify the phonon number. $\tilde{\mathcal{G}}^{ii}_{33}$ for example is the updated GREENS function from position 3 with i phonons to position 3 with i phonons. These terms do not describe multiphoton excitation between the existing block and the new slice. The full series can be written as a fraction

$$\begin{aligned}\left(\tilde{\mathcal{G}}^{ii}_{33}\right)^{-1} =& E - \mathcal{H} - \mathcal{H}_I^{\dagger}\mathcal{G}^{ii}_{22}\mathcal{H}_I\\ &- \delta^{\dagger}\left(\mathcal{G}^{(i+1)i}_{22} + \mathcal{G}^{(i-1)i}_{22}\right)\mathcal{H}_I - \mathcal{H}_I^{\dagger}\left(\mathcal{G}^{i(i+1)}_{22} + \mathcal{G}^{i(i-1)}_{22}\right)\delta\\ &- \delta^{\dagger}\left(\mathcal{G}^{(i+1)(i+1)}_{22} + \mathcal{G}^{(i-1)(i-1)}_{22}\right)\delta\end{aligned}$$

The off-diagonal elements are the paths which start at position 3 with i phonons and come back with j phonons. With the help of the diagonal elements we can compute the off-diagonal elements

$$\begin{aligned}\tilde{\mathcal{G}}^{ij}_{33} = \tilde{\mathcal{G}}^{ii}_{33}\mathcal{H}_I^{\dagger}\mathcal{G}^{ij}_{22}\mathcal{H}_I\tilde{\mathcal{G}}^{jj}_{33} &+ \tilde{\mathcal{G}}^{ii}_{33}\delta^{\dagger}\left(\mathcal{G}^{(i+1)j}_{22} + \mathcal{G}^{(i-1)j}_{22}\right)\mathcal{H}_I\tilde{\mathcal{G}}^{jj}_{33}\\ &+ \tilde{\mathcal{G}}^{ii}_{33}\mathcal{H}_I^{\dagger}\left(\mathcal{G}^{i(j+1)}_{22} + \mathcal{G}^{i(j-1)}_{22}\right)\delta\tilde{\mathcal{G}}^{jj}_{33}\end{aligned}$$

The GREEN's function $\tilde{\mathcal{G}}^{ij}_{31}$ and $\tilde{\mathcal{G}}^{ij}_{13}$ are obtained by

$$\begin{aligned}\tilde{\mathcal{G}}^{ij}_{31} &= \tilde{\mathcal{G}}^{ii}_{33}\left(\mathcal{H}_I^{\dagger}\mathcal{G}^{ij}_{22} + \delta^{\dagger}\left(\mathcal{G}^{(i+1)j}_{22} + \mathcal{G}^{(i-1)j}_{22}\right)\right),\\ \tilde{\mathcal{G}}^{ij}_{13} &= \left(\mathcal{G}^{ij}_{22}\mathcal{H}_I + \left(\mathcal{G}^{i(j+1)}_{22} + \mathcal{G}^{i(j-1)}_{22}\right)\delta\right)\tilde{\mathcal{G}}^{jj}_{33}.\end{aligned}$$

Unfortunately, this is still unstable.

❧

References

[1] Antoine de Saint-Exupèry. *Terre des hommes*. Le Livre de Poche, 1939.

[2] Bjorken, J., and Drell, S. *Relativistic quantum mechanics*. International series in pure and applied physics. McGraw-Hill, 1964.

[3] Bringhurst, R. *The Elements of Typographic Style*. Hartley & Marks, 2013.

[4] Caignaert, C. Kp-Fonts, 2011.

[5] Datta, S. *Electronic Transport in Mesoscopic Systems*. Cambridge Studies in Semiconductor Physics and Microelectronic Engineering. Cambridge University Press, 1997.

[6] Fano, U. Effects of configuration interaction on intensities and phase shifts. *Phys. Rev. 124* (Dec 1961), 1866–1878.

[7] Ferry, D., Goodnick, S., and Bird, J. *Transport in Nanostructures*. Cambridge University Press, 2009.

[8] Feuersänger, C. Manual for Package pgfplots, 2012.

[9] Gómez-León, A., and Platero, G. Floquet-bloch theory and topology in periodically driven lattices. *Phys. Rev. Lett. 110* (May 2013), 200403.

[10] Grassi, R., Gnudi, A., Gnani, E., Reggiani, S., and Baccarani, G. Mode space approach for tight binding transport simulation in graphene nanoribbon fets. *IEEE Transactions on Nanotechnology 10*, 3 (May 2011), 371–378.

[11] Grassi, R., Gnudi, A., Imperiale, I., Gnani, E., Reggiani, S., and Baccarani, G. Mode space approach for tight-binding transport simulations in graphene nanoribbon field-effect transistors including phonon scattering. *Journal of Applied Physics 113*, 14 (2013), 144506.

[12] Grosso, G., and Parravicini, G. *Solid State Physics*. Elsevier Science, 2013.

[13] Guo, Jing; Datta, S. L. M. A. M. P. Towards Multi-Scale Modeling of Carbon Nanotube Transistors. *eprint arXiv:cond-mat/0312551* (2003).

[14] Joe, Y. S., Satanin, A. M., and Kim, C. S. Classical analogy of fano resonances. *Physica Scripta 74*, 2 (2006), 259.

[15] Knuth, D. *The TeXbook*. Computers & typesetting. Addison-Wesley Publishing Company, 1984.

[16] Lamport, L. *LATEX: a document preparation system*. Addison-Wesley Pub. Co., 1986.

[17] Lehoucq, R., Sorensen, D., and Yang, C. Arpack users' guide: Solution of large scale eigenvalue problems with implicitly restarted Arnoldi methods, 1997.

[18] Libisch, F. *Electronic structure and transport in mesoscopic devices*. PhD thesis, Vienna University of Technology, 2008.

[19] Libisch, F., Rotter, S., Güttinger, J., Stampfer, C., and Burgdörfer, J. Transition to landau levels in graphene quantum dots. *Phys. Rev. B 81* (Jun 2010), 245411.

[20] Luisier, M., Schenk, A., and Fichtner, W. Quantum transport in two- and three-dimensional nanoscale transistors: Coupled mode effects in the nonequilibrium green's function formalism. *Journal of Applied Physics 100*, 4 (2006), 043713.

[21] McCann, E. Electronic properties of monolayer and bilayer graphene.

[22] Miroshnichenko, A. E., Flach, S., and Kivshar, Y. S. Fano resonances in nanoscale structures. *Rev. Mod. Phys. 82* (Aug 2010), 2257–2298.

[23] Pierrat, R., Ambichl, P., Gigan, S., Haber, A., Carminati, R., and Rotter, S. Invariance property of wave scattering through disordered media. *Proceedings of the National Academy of Sciences 111*, 50 (2014), 17765–17770.

[24] Rotter, S., Libisch, F., Burgdörfer, J., Kuhl, U., and Stöckmann, H.-J. Tunable fano resonances in transport through microwave billiards. *Phys. Rev. E 69* (Apr 2004), 046208.

[25] Sanvito, S. *Giant Magnetoresistance and Quantum Transport in Magnetic Hybrid Nanostructures*. PhD thesis.

[26] Tantau, T. The Tikz and pgf Packages, 2010.

[27] Tufte, E. *Beautiful Evidence*. Graphics Press, 2006.

[28] Wang, J., Polizzi, E., and Lundstrom, M. A three-dimensional quantum simulation of silicon nanowire transistors with the effective-mass approximation. *Journal of Applied Physics 96*, 4 (2004), 2192–2203.

[29] Wiener, A. D., and Kindermann, M. Signatures of evanescent mode transport in graphene. *Phys. Rev. B 84* (Dec 2011), 245420.

[30] Wilson, P., and Madsen, L. The Memoir Class for Configurable Typesetting. The Herries Press, 20009.

◆